Results in Engineering 30 (2026) 110492

Contents lists available at ScienceDirect

Results in Engineering

journal homepage: www.sciencedirect.com/journal/results-in-engineering

Research paper

Analytical approach for the characterization of the chemical and mineralogical composition of Al_2O_3–SiO_2–CaO–MnO–Li_2O–type lithium-ion battery (LIB) slags

Marko Ranneberg [a], Hans-Eike Gäbler [a], Simon Goldmann [a], Wilhelm Nikonow [a], Jens Götze [b], Haojie Li [c], Michael Fischlschweiger [d], Torsten Graupner [a,*]

[a] Federal Institute for Geosciences and Natural Resources (BGR), 30655 Hannover, Germany
[b] TU Bergakademie Freiberg, Institute of Mineralogy, 09596 Freiberg, Germany
[c] Clausthal University of Technology, Institute of Energy Process Engineering and Fuel Technology, 38678 Clausthal-Zellerfeld, Germany
[d] Karlsruhe Institute of Technology, Institute of Technical Thermodynamics, 76131 Karlsruhe, Germany

ARTICLE INFO

Keywords:
Slag characterization
LIBs recycling
Li recovery
Engineering of artificial minerals
γ-$LiAlO_2$
Luminescence
Amorphous constituents

ABSTRACT

The process for economic recovery of Li from slags produced during the recycling of lithium-ion batteries via a combined pyro- and hydrometallurgical process route needs to be optimized. This requires a detailed knowledge of the phase composition, metal distribution, and microstructure of the produced slags. In this work, a new two-stage analytical approach is presented, which enables the geochemical, mineralogical, and structural investigation of these slags. The methodology was developed on samples of the model system Al_2O_3–SiO_2–CaO–MnO–Li_2O and is demonstrated here on an artificial Li- and Mn-rich slag sample.

Rapid analytical methods (short-wave ultraviolet radiation and micro energy-dispersive X-ray fluorescence spectroscopy) are adapted for on-site recycling process monitoring. They are validated by state-of-the-art mineralogical (X-ray diffraction with Rietveld quantitative phase analysis), bulk chemical (X-ray fluorescence, inductively coupled plasma mass spectrometry), and microanalytical (electron probe microanalysis, scanning electron microscopy-based automated mineralogy, laser ablation inductively coupled plasma-time-of-flight mass spectrometry) techniques. Apparently contradictory results of the latter techniques are discussed and reconciled.

The integration of the new routine and rapid analytical methods into the pyro- and hydrometallurgical recycling route for lithium-ion batteries will be discussed considering the key mineralogical questions to be answered in process development, industrial process control, and process route adaptation.

1. Introduction

The intensive use of lithium-ion batteries (LIBs) in various electronic devices and the forecasted increasing electrification of the transportation sector will lead to a steady return of spent LIBs in the coming years [1,14,42,49]. From 2026, at least 65 % of the average weight and from 2028 a minimum of 50 % of the Li content of these batteries has to be recycled in the EU according to the new battery regulation 2023/1542 annex XII, part B [50]. By this time at the latest, a wide spectrum of batteries with different housings, cell chemistries and sizes must be fed into suitable recycling processes in order to recover most of the valuable materials they contain. A lithium-ion battery (LIB) generally consists of an anode (usually graphite) bound on a copper conductor plate, a cathode ($LiCoO_2$ (LCO-type), $Li(Ni_xMn_yCo_{1-x-y})O_2$ (NMC-type), $LiMn_2O_4$ (LMO-type), $Li(Ni_xCo_yAl_{1-x-y})O_2$ (NCA-type) or $LiFePO_4$ (LFP-type)) bound on an aluminium conductor plate, a binder (polyvinylidene fluoride), an electrolyte (usually propylene carbonate, ethylene carbonate or dimethyl sulfoxide with Li salts like $LiPF_6$, $LiBF_4$, $LiCF_3SO_3$ or $Li(SO_2CF_3)_2$), a separator (polyethylene or polypropylene) and an external case (aluminium, steel, plastic) [3,13,30,53,57]. Due to the complexity of the batteries, the development of an economic and ecologic recycling process represents a major challenge [27]. Currently, pyrometallurgy with subsequent hydrometallurgical refining is the predominant method to recycle spent LIBs in the industry [28] with a worldwide annual capacity of >160,000 t/a [54]. The procedure can basically handle all common battery types without pre-sorting, but is so

* Corresponding author.
E-mail address: torsten.graupner@bgr.de (T. Graupner).

https://doi.org/10.1016/j.rineng.2026.110492
Received 25 February 2025; Received in revised form 13 March 2026; Accepted 9 April 2026
Available online 12 April 2026

far only economic for battery types with cathodes containing Co and Ni [13], such as NMC, LCO and NCA. The process route comprises only two steps. In the first process step, spent LIBs are dismantled to the module level or shredded and subsequently fed into a high temperature furnace with coke as well as slag formers like limestone ($CaCO_3$) and quartz sand (SiO_2) [13,45,51]. The anode, electrolyte, plastics and separator are burned and generate a part of the energy needed for smelting [6,36]. After smelting, Li and other base metals like Al and Mn are largely transferred into a slag that is rich in Ca and Si [13]. The valuable metals Co, Cu, Ni, and also Fe are reduced to an alloy [5,19,55]. During a second process step, pure metals are recovered from the alloy by hydrometallurgical refining [56]. The slag is usually disposed of or sold as construction material [51]. Lithium as the most valuable metal in these slags cannot be recovered efficiently, because the element is heterogeneously distributed among various silicates and oxides depending on the chemical composition of the melt. This prevents effective separation and consequently the economic recovery.

To meet the ambitious targets set by the new EU Battery Regulation 2023/1542, a sustainable process for recovering Li from slag must be developed. In addition to the recovery of Li as LiCl from flue gases [44], the "Engineering of Artificial Minerals" (EnAM) strategy - successfully applied to LIB slags in the PyroLith research project [23,37,38,41] - represents a promising approach. The aim of the latter concept is to transfer the entire Li content of the melt into the artificial Li-rich phase γ-$LiAlO_2$ (Li = 10.5 wt%) by optimizing the slag composition. After cooling and comminution of the slag, γ-$LiAlO_2$ can be effectively separated from other slag components by froth flotation [25]. Lithium and a part of the Al can subsequently be recovered from the γ-$LiAlO_2$ concentrate by leaching and precipitation.

Thermodynamic modeling, especially the **cal**culation of **pha**se **d**iagrams (CALPHAD) framework [26,43], plays a vital role within the EnAM strategy in designing and optimizing slag compositions in order to enable a higher Li transfer rate into the target phase [24]. Several studies [40,46,47] have recently applied thermodynamic simulations under CALPHAD framework [2] to calculate and predict the solidified phases of Li-containing slags. Qualitatively, most of the major phases can be well predicted. However, quantitatively predicted mineral phase contents and solidification sequences need to be further developed and validated in the future. Particularly, experimental data for some solid solutions, such as the $MnAl_2O_4$–$LiAl_5O_8$ solid solution, are not yet sufficiently available in the literature. In this regard, detailed analytical investigations of the slag samples are essential to generate, evaluate, further refine, and validate thermodynamic databases. Especially the quantitative chemical and mineralogical composition of samples, with consideration of Li evaporation, solubility behavior and crystallization sequence are key examinations for further optimization. However, appropriate analysis methods are very time-consuming due to the high preparative and instrumental effort involved. They are therefore only suitable to a limited extent for in-process analyses, such as checking the content, distribution, grain size, and crystal shape of the target phase γ-$LiAlO_2$ in slag samples or assessing the separation efficiency during froth flotation. For these areas of application, methods for rapid analysis need to be developed that can provide information on the content of the main slag phases and the microstructure of the slags within a few hours.

In this study, we present an analytical approach to fully characterize and validate the chemical and mineralogical composition of Al_2O_3–SiO_2–CaO–MnO–Li_2O-type LIB slags with electron beam, mass spectrometric and X-ray diffraction techniques. The results will be used to validate two rapid analysis methods based on micro energy-dispersive X-ray fluorescence analysis (μ-EDXRF) and short-wave ultraviolet radiation (UVC radiation), which can be applied as in-process instruments to evaluate the relative content, distribution, grain size, and crystal shape of individual slag phases in large samples within a few seconds (UVC radiation) or a few hours (μ-EDXRF), respectively. The aim of this work is to provide an analytical toolbox that can be utilised along the entire process chain and from which an appropriate analysis method can be selected depending on the desired detailed information. In order to make the paper more accessible to readers less familiar with the topic, Table 1 outlines the slag phases discussed in this study.

2. Materials and methods

2.1. Sample preparation

In total, 50 samples from the artificial slag system Al_2O_3–SiO_2–CaO–MnO–Li_2O and real NMC-type LIB slags, ranging in weight from 50 g to 100 kg, were prepared in the frame of the PyroLith project. To demonstrate the analytical approach for chemical and mineralogical characterization of LIB slags, an artificial slag sample of known chemical composition (Table 2) with 11.5 wt% Li_2O and 10.1 wt % MnO was selected. The slag (100 g) was produced by the Institute of Metallurgy and Metal Recycling (IME) at RWTH Aachen University. The chemical composition of the sample is largely within the compositional range of the so-called Li-rich metallurgical slag claimed by UMICORE in the patent WO 2017/121663 A1 [39] for the economic recovery of Li (Table 2). The slag was produced in a Nabertherm high-temperature resistance furnace (HT 160/17) under strong reducing conditions in an isostatic graphite crucible (ø 65/55 mm × 130 mm) using pure (≥98 %) Li_2CO_3, MnO, CaO (Sigma Aldrich), Al_2O_3 (Nabalox) and SiO_2 (Sibelco IOTA) as starting materials. The sample was heated up to 1500 °C with 500 °C/h, held at the target temperature for 45 minutes under an Ar atmosphere, then cooled inside the furnace at a controlled rate of 25 °C/h under ambient atmosphere. No surface oxidation was observed during the cooling process, and subsequent analyses did not indicate any signs of oxidation.

2.2. Analytical methods

2.2.1. Bulk analytical methods

The chemical bulk sample composition excluding Li was measured in glass beads with a wavelength-dispersive PANanlytical Axios X-ray fluorescence (XRF) spectrometer. The measurement was performed with a Rh tube. Certified international reference samples were used to calibrate the device. The evaluation and matrix correction was carried out using the method of De Jongh [8]. For the analysis, 1 g of the finely ground sample was annealed at 750 °C in a porcelain crucible to release

Table 1
List of slag phases discussed in this study.

Phase	Chemical Formula	Comment
Gehlenite	$Ca_2Al_2SiO_7$	Ca endmember of the melilite solid solution series
γ-$LiAlO_2$	$LiAlO_2$	Artificial target phase of the Li enrichment
Glaucochroite	$CaMnSiO_4$	Member of the monticellite-kirschsteinite series
β-Eucryptite	$LiAlSiO_4$	Member of the phenakite series
Li_2MnSiO_4	$Li_{1.81}Na_{0.01}Ca_{0.01}Mg_{0.02}Mn_{0.74}Al_{0.19}Si_{1.03}O_4$	Li_2MnSiO_4- β-eucryptite solid solution
Mixed phase I	$Li_{3.11}Na_{0.01}Mg_{0.02}Mn_{0.84}Al_{1.05}Si_2O_8$	Mixture of Li_2MnSiO_4 and β-eucryptite, detected by SEM-MLA, EPMA and LA-ICP-TOFMS
Mixed phase II	$Li_{0.97}Na_{0.01}Mg_{0.01}Ca_{0.82}Mn_{1.04}Al_{1.1}Si_2O_8$	Close intergrowth of β-eucryptite and glaucochroite, detected by SEM-MLA, EPMA and LA-ICP-TOFMS
Fringe area of gehlenite	$Li_{1.07}Na_{0.2}Ca_{2.44}Mg_{0.06}Mn_{0.97}Al_{2.49}Si_{3.58}O_{15}$	Fringes around gehlenite, detected by LA-ICP-TOFMS
Fringe area of γ-$LiAlO_2$	$Li_{0.89}Na_{0.03}Ca_{0.03}Mn_{0.05}Al_{0.69}Si_{0.22}O_2$	Fringes around γ-$LiAlO_2$, detected by LA-ICP-TOFMS

Table 2
Initial composition (calculated from the weights of the pure substances before melting) of the examined slag sample compared to the composition of the Li-rich metallurgical slag claimed by UMICORE in the patent WO 2017/121,663 [39] in wt%.

	Li_2O	Al_2O_3	SiO_2	CaO	MnO
slag sample	11.5	37.5	25.0	15.9	10.1
UMICORE slag	3 - 20	38 - 65	<45	<55	1 - 7

volatile components and measure the loss on ignition. The annealed sample was then mixed with 5 g of lithium metaborate and melted in platinum crucibles at 1200 °C to form glass beads.

The Li content was determined by inductively coupled plasma mass spectrometry (ICP-MS, PlasmaQuant MS Elite, Analytik Jena, Germany) after acid dissolution of the slag. Fifty mg of the finely ground sample were exactly weighed into an aluminium crucible and quantitatively transferred into a digestion polytetrafluoroethylene (PTFE) crucible where ten drops of deionised water (>18 MΩ) have been placed before. The digestion crucible is closed after addition of 0.5 ml nitric acid (65 wt %) and 4 ml hydrofluoric acid (48 wt%), heated up to 170 °C within 2 h, and kept at this temperature for 24 h. After cooling, 1 ml of nitric acid (65 wt%) is added and this liquid is evaporated to dryness by the following procedure: Heating up to 90 °C within 30 min, keeping at this temperature for 30 min, heating up to 110 °C within 12 min, keeping at this temperature for 30 min, heating up to 120 °C within 30 min, and keeping at this temperature for 15 h. During the evaporation step, a PTFE cap with a small hole connected to a vacuum pump covers the crucible. The pump is protected by two washing bottles containing a sodium hydroxide solution for the absorption of the acidic fumes. After cooling, 5 ml of hydrochloric acid (6 M) is added to the evaporated residue. The digestion crucible is closed again, heated up to 150 °C within 2 h and kept at this temperature for 20 h. After cooling, the obtained solution is transferred into a Falcon tube and made up to 50 ml by deionised water. This solution is diluted 1:1000 with nitric acid (0.29 M) to obtain the solution used for Li determination by Q-ICP-MS (external calibration using 10, 20, and 40 μg Li/L calibration solutions). Analytical quality control for the above given procedure was done by repeated analysis of the candidate reference sample zinnwaldite ZW-C [17] within each analytical sequence. The Li_2O content of ZW-C obtained is 2.44 ± 0.04 wt% ($n = 7$), which is in good agreement with the reference value for ZW-C of 2.43 wt% Li_2O given in Govindaraju et al. [17].

The quantitative mineralogical composition of the sample was determined by X-ray diffraction (XRD) using a PANalytical X'Pert Pro MPD X-ray diffractometer in reflection geometry with Co-Kα radiation (40 kV and 40 mA), a variable divergence slit (20 mm irradiated length), primary and secondary soller slits (0.04 rad), anti-scatter slits, a fixed incident beam mask (10 mm), a diffracted beam monochromator, and a point detector. The finely ground sample was transferred into the sample holder using the backloading preparation method. An overview measurement to determine the qualitative phase composition was carried out in the angular range of 5° to 80° 2θ with a step size of 0.03° 2θ and a measurement time of 3 s per step. The measurement to quantify the phase content was performed in the angular range of 5° to 85° 2θ, a step size of 0.03° 2θ and a measurement time of 15 s per step. The amorphous constituents were determined by adding 20 wt% rutile (standard reference material NIST No 674a) to the sample as internal standard. The software X'pert High Score Plus and the PDF-2 database from the International Centre for Diffraction Data (ICDD) were utilised to identify the slag phases. The Rietveld refinement was done with the Profex/BGMN [10] software (suite 5.2.9) using the included crystal structure database (rutile) and additional crystal structure data for β-eucryptite [34], γ-$LiAlO_2$ [29], glaucochroite [22], Li_2MnSiO_4 [35], and gehlenite [48].

2.2.2. Microanalytical methods

The quantitative chemical compositions of the slag phases in carbon-coated polished sections of the slag sample were analysed with a JEOL JXA-8530F field emission microprobe by wavelength-dispersive spectrometry (WDX). The instrument was set to an acceleration voltage of 10 kV and a beam current of 20 nA. The spot size of the electron beam was either 1 or 10 μm depending on the grain size of the phase of interest. The respective X-ray lines, standards, measuring times and spectrometer crystals for each element were as follows: Na Kα, jadeite, 10 s, TAPH; Mg Kα, periclase, 30 s, TAPH; Al Kα, corundum, 15 s, TAP; Si Kα, orthoclase, 10 s, TAP; K Kα, orthoclase, 20 s, PETH; Ca Kα, wollastonite, 30 s, PETH; Mn Kα, Mn metal, 30 s, LIFL; Fe Kα, hematite, 20 s, LIFL. Except for Si, the mean atomic number (MAN) correction [11] of the ProbeSoftware package was applied with background raw data corrected using the phi-rho-Z method supplied by ProbeSoftware package. Linear off-peak background correction was applied for Si with 5 s counting time for each background.

Scanning electron microscope (SEM) analyses were carried out to investigate the microstructure of the slag sample in carbon-coated polished sections. The measurements were conducted under high vacuum with 25 kV on an MLA Quanta 650F field emission gun SEM (FE-SEM) from FEI equipped with two Bruker Quantax X-Flash 5030 energy-dispersive X-ray spectrometers (EDX) and Mineral Liberation Analysis (MLA) software (suite 3.1.4), allowing fully automated quantitative evaluations. The MLA software uses the EDX system of the SEM combined with backscattered electron (BSE) imaging for automatic identification of mineral phases. Mineral particles are identified by their specific grey value in the BSE image after removal of the background (i.e. epoxy resin). Within identified particles, EDX measurements are performed and the characteristic X-ray spectrum of each analysis spot is compared with the X-ray spectra of defined phases stored in a database. In this work the GXMAP mode was utilised to obtain a continuous mapping of the sample. Further details on the device and the measurement modes can be found in the literature [12,18].

Laser ablation inductively coupled plasma time-of-flight mass spectrometry (LA-ICP-TOFMS) was applied to provide a quantified element distribution map (Li, Na, Mg, Al, Si, Ca, Mn) with a spatial resolution of 5 μm for a subarea (~11 mm^2) of the polished section prepared from the slag material. The LA-ICP-TOFMS system uses the 193 nm laser ablation system IRIDIA (Teledyne CETAC Technologies, Omaha, USA) and an icpTOF 2R inductively coupled plasma time-of-flight mass spectrometer (TOFWERK AG, Thun, Switzerland). The IRIDIA system is equipped with a fast washout Cobalt Sample Cell and an Aerosol Rapid Introduction System (ARIS). The laser ablation system is controlled by the software Chromium 3.1 (Teledyne CETAC Technologies, Omaha, USA) while the mass spectrometer is controlled by the software TOFpilot (TOFWERK AG, Thun, Switzerland). Data evaluation is done using the software HDIP 1.7 (Teledyne CETAC Technologies, Omaha, USA). Two He gas flows of 0.34 L/min and 0.29 L/min for the body and the inner cell of the Cobalt Sample Cell, respectively, transport the ablated sample material into the torch of the mass spectrometer. A special tune setting was used for the ICP-TOFMS to cover the mass range from 7 to about 90 atomic mass units (amu). The sample material was ablated by a 5 μm square shaped laser beam at a fluence of 5 J/cm^2 with a repetition rate of 120 Hz and a dosage of 1 pulse/spot resulting in a scan speed of 600 μm/s. In this way an area of about 5 mm × 2 mm is gapless ablated for a single map in about two hours. Ten gas blanks and 10 lines on a calibration material (CM) were recorded at equally distributed time intervals together with the sample. The CM was prepared from an aliquot of a comparable slag material which was wet ground in a planetary ball mill (Planetary Micro Mill PULVERISETTE 7 premium line, Fritsch, Idar-Oberstein, Germany) using 3 mm agate balls and an agate grinding bowl. After grinding and freeze drying the material was characterized by XRF (Na, Mg, Al, Si, Ca, Mn) and ICP-MS (Li) after wet digestion. For the use as a CM in LA-ICP-TOFMS, the obtained powder was pressed to a pellet. Raw data of the TOF instrument were imported into the HDIP software for further processing. After

background correction based on the recorded gas blanks, element distribution maps in counts per second (cps) were calculated. The conversion of these maps into concentration-related element distribution maps is based on the records of the CM. To account for different ablation yields of sample (slag material) and CM (pressed powder pellet) external calibration with internal standardization is applied. The known sum of the concentrations of the oxides Li_2O, Na_2O, MgO, Al_2O_3, SiO_2, CaO, and MnO for the CM and the assumption that the sum of those oxides is equal to 100 wt% for the sample are used as internal standard. Regions of the ablated sample surface with similar geochemical composition are identified afterwards by cluster analysis (K-means algorithm). For each 5 μm square pixel element concentrations are available and based on the contents of the elements Li, Al, Si, Ca, and Mn eight clusters were calculated. The number of calculated clusters was chosen as the minimum number of clusters that are necessary to separate the two LiCaMnAlSi-phases (mixed phase I and II), which are well distinguishable in the BSE images.

2.2.3. Rapid analytical methods

The distribution of the element contents in a cross section through the slag sample was investigated with spatially resolving micro energy-dispersive X-ray fluorescence spectroscopy (μ-EDXRF) using a M4 Tornado Plus from Bruker and tested as a rapid analysis method to visualize individual slag phases. Micro-EDXRF is an investigation method that can detect elements with an atomic number as low as 6 (C) and higher in the used configuration. The device is equipped with a Rh tube (excitation energy of 50 kV and 600 μA) and two silicon drift detectors. The X-ray beam is focused via a polycapillary lens, resulting in a measuring spot size of about 20 μm. The M4 Tornado Plus can be used to analyse sawn or polished samples with dimensions of up to 16 cm × 20 cm. For the analysis, the above-mentioned polished sample section was used. The sample was measured with a step size (pixel size) of 20 μm and a measurement time of 5 ms per step with a total resolution of 1500 × 1500 pixels resulting in a total measurement time of about 3 h. The results of the measurement were evaluated using the M4 Tornado software from Bruker. They can be visualized as element distribution maps with colour- or greyscale-coded element intensities [32,33].

In addition to μ-EDXRF, short-wave ultraviolet radiation (UVC radiation, 254 nm) was also tested as a rapid analysis method for visualisation of the target phase γ-$LiAlO_2$. For the investigation, the UV lamp Raytector (R5-FLS) from Raytech Industries (CT, USA) and a commercially available digital camera (resolution up to 40 MP) with tripod was used. The fluorescent tubes integrated in the lamp generate 6 W short-wave (254 nm) and 6 W long-wave power (400 nm). They can be used separately or simultaneously.

In order to examine the source of the luminescence of γ-$LiAlO_2$, spectral cathodoluminescence (CL) investigations were carried out at TU Bergakademie Freiberg on carbon-coated, polished thin sections using a HC1-LM "hot cathode" microscope [31]. The system operates at an acceleration voltage of 14 kV and a current of 0.2 mA (current density approx. 10 μA/mm^2). Luminescence microphotographs were taken directly during the CL examinations with a Peltier-cooled digital video camera (OLYMPUS DP72) using the Stream Start 1.7 software. Spectral CL measurements were carried out with a spot diameter of 30 μm and a measurement time of 1 s in a wavelength range of 370 to 900 nm using a digital Acton Research SP-2356 triple grating spectrograph with a Princeton Spec-10 CCD detector, which was coupled to the microscope via an adapter using a fibre optic cable. The wavelength calibration was done with a mercury lamp. For data collection, storage and processing operations the software WinSpec Version 2.5 was used.

3. Results

3.1. Bulk analytical methods

3.1.1. XRF and ICP-MS

The chemical composition of the examined slag, measured by XRF (Al_2O_3, SiO_2, CaO, MnO, MgO, Na_2O) and ICP-MS (Li_2O), is summarized in Table 3. In addition to the main oxides Al_2O_3, SiO_2, CaO, MnO, and Li_2O, minor concentrations of MgO and Na_2O were also detected. The sum of the quantified oxides is 99.88 wt% and the loss of ignition (LOI) is 0.93 wt%.

3.1.2. Rietveld quantitative phase analysis

The Rietveld refinement of the investigated slag sample with 20 wt% rutile as internal standard is illustrated in Fig. 1. The figures of merit of the refinement (R_{wp}, R_{exp}, χ^2) as well as the difference plot demonstrate a good agreement between observed and calculated intensity values.

The results of the Rietveld quantitative phase analysis are listed in Table 4. They show that the investigated slag is composed of five crystalline phases from the mineral groups of silicates and oxides in addition to amorphous constituents. The crystalline phases account for around three-quarters of the sample, while approximately one-quarter is amorphous. Three crystalline slag phases contain lithium: γ-$LiAlO_2$ (target phase for Li enrichment), β-eucryptite (β-$LiAlSiO_4$) and Li_2MnSiO_4. The remaining crystalline phases are lithium-free: gehlenite ($Ca_2Al_2SiO_7$) and glaucochroite ($CaMnSiO_4$).

3.2. Microanalytical methods

3.2.1. EPMA

The average chemical compositions of the slag phases contained in the examined sample, determined by electron probe micro analysis (EPMA), and the calculated formulas of the solid solutions and mixed phases are summarized in Table 5. Lithium cannot be measured by WDX using EPMA and O is calculated by stoichiometry. Therefore, all elements were considered as oxides with fixed stoichiometry. Manganese was assumed to be present exclusively as MnO, based on the strongly reducing conditions during sample preparation. The Li_2O content was calculated by difference, using the deviation from a 100 % total and the known stoichiometry of the corresponding phases. For the investigation a total of 171 spot analyses were carried out. Seven slag phases are distinguished: gehlenite, γ-$LiAlO_2$, glaucochroite, β-eucryptite, Li_2MnSiO_4, mixed phase I (composed of a mixture of β-eucryptite and Li_2MnSiO_4), and mixed phase II (close intergrowth of glaucochroite and β-eucryptite). The ternary diagram Al_2O_3-SiO_2-CaO + MnO in Fig. 2 depicts the variation in the chemical composition of the solid solutions and mixed phases.

3.2.2. SEM-MLA

The results of the microstructure analysis using SEM and MLA are presented below. A backscattered electron (BSE) image of a cross section through one-half of the entire sample is shown in Fig. 3, while Fig. 4 displays the associated colour-coded phase distribution image by MLA. Selected details at two different magnifications are presented in Fig. 5. The BSE images and the colour-coded phase distribution image indicate that the slag is solidified in a vesicular to compact, dense to medium-grained, hypocrystalline, heterogeneous microstructure with a silicate matrix. The upper rim area, which represents the top of the sample, is notably poor in the target phase γ-$LiAlO_2$. This part consists mainly of gehlenite, mixed phase II, and Li_2MnSiO_4. The groundmass in the remaining part of the slag contains large crystals of γ-$LiAlO_2$, gehlenite, and Li_2MnSiO_4. The main phase γ-$LiAlO_2$ crystallized as euhedral grains in the upper part, but as dendritic grains in the middle and lower parts of the sample. The grain size of γ-$LiAlO_2$ is between 5 and 500 μm. However, dendritic γ-$LiAlO_2$ crystals reach lengths of up to 5 mm. Gehlenite crystallized as skeletal to dendritic grains in the range of 10 μm to 2.5 mm. In contrast to gehlenite and γ-$LiAlO_2$, Li_2MnSiO_4 forms euhedral crystals in all parts of the sample with grain sizes between 20 and 200 μm (Fig. 5a). The matrix of the slag consists of mixed phase II and to a lesser extent of mixed phase I. These phases are cryptocrystalline and fill the interstices between the main and minor slag phases. Mixed phase I is chemically a mixture of β-eucryptite and Li_2MnSiO_4. The phase is

Table 3
Chemical composition of the investigated slag sample measured by XRF/ICP-MS in wt%.

Al_2O_3	SiO_2	CaO	MnO	Na_2O	MgO	sum XRF	Li_2O	Total	LOI
38.8	24.6	16.4	10.2	0.02	0.16	90.18	9.7	99.88	0.93

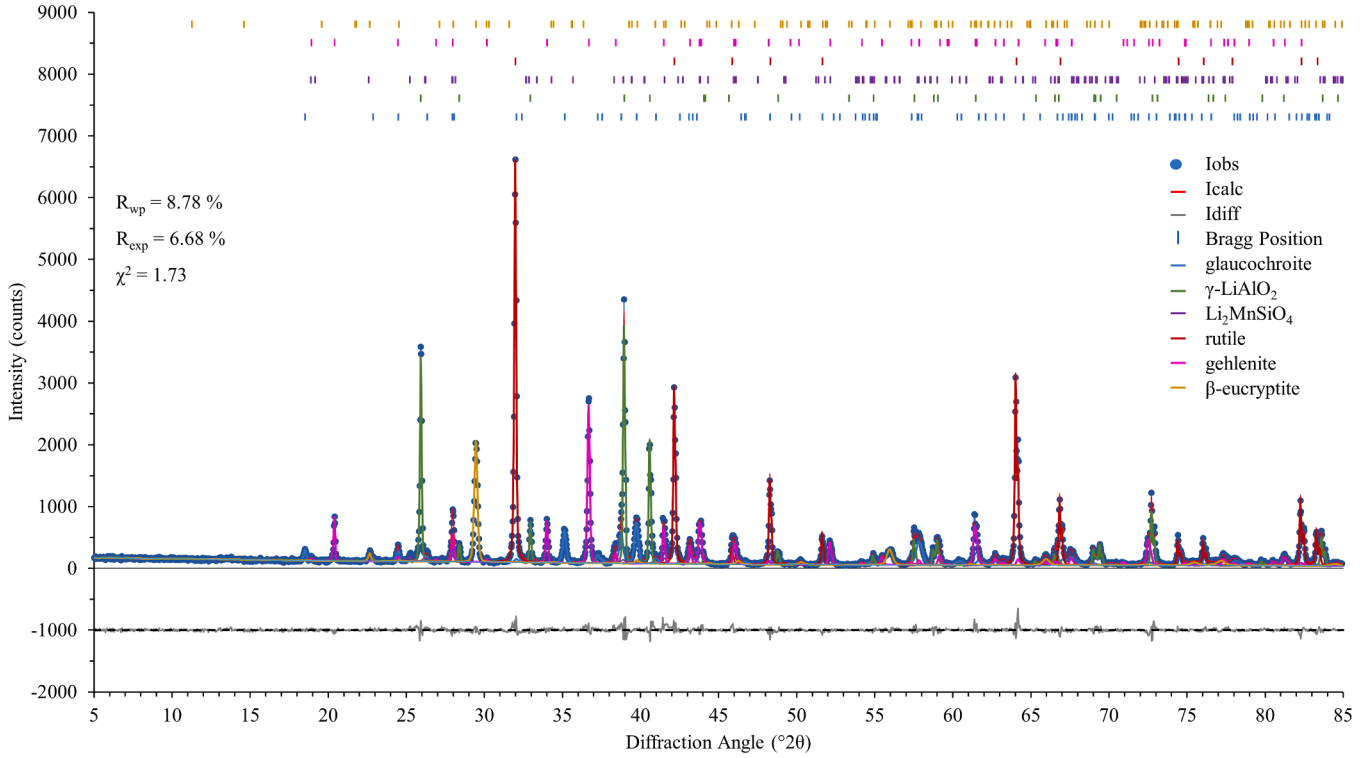

Fig. 1. Rietveld refinement of the analysed slag sample with 20 wt% rutile (TiO_2) as internal standard.

Table 4
Quantitative phase composition of the analysed sample obtained from Rietveld analysis in wt%. Values in parentheses represent twice the estimated standard deviation (2σ) given by Profex/BGMN.

gehlenite	γ-$LiAlO_2$	glaucochroite	β-eucryptite	Li_2MnSiO_4	amorphous	Total
20 (0.7)	29 (2.4)	12 (0.5)	7 (0.4)	4 (0.5)	28 (2.6)	100

Table 5
Average chemical composition of slag phases contained in the analysed slag in wt% and calculated formulas of the solid solutions and mixed phases from EPMA. *Li_2O content in wt% estimated from the deficit in the mass balance and the stoichiometric composition of the respective phase, which was used to calculate the mineral formulas. n = number of spot analyses. bdl = below detection limit.

Phase	Li_2O*	Al_2O_3	SiO_2	CaO	MnO	Na_2O	MgO	K_2O	FeO	Total
gehlenite	-	32.3	25.4	39.0	2.0	0.1	0.1	bdl	bdl	98.9
$n = 31$		$\mathbf{Ca_{1.93}Na_{0.01}Mn_{0.08}Mg_{0.01}Al_{1.76}Si_{1.17}O_7}$								
γ-$LiAlO_2$	21.1	71.7	5.1	bdl	0.2	bdl	bdl	bdl	bdl	98.1
$n = 54$		$\mathbf{Li_{0.94}Al_{0.94}Si_{0.06}O_2}$								
glaucochroite	-	1.8	31.8	27.9	35.7	bdl	0.2	bdl	bdl	97.4
$n = 2$		$\mathbf{Ca_{0.94}Mg_{0.01}Mn_{0.95}Al_{0.07}SiO_4}$								
β-eucryptite	11.7	41.2	49.2	0.2	0.6	bdl	bdl	bdl	bdl	102.9
$n = 2$		$\mathbf{Li_{0.95}Al_{0.99}Mn_{0.01}Si_{1.01}O_4}$								
Li_2MnSiO_4	16.7	5.9	38.1	0.2	32.2	0.1	0.4	bdl	bdl	93.6
$n = 19$		$\mathbf{Li_{1.81}Na_{0.01}Ca_{0.01}Mg_{0.02}Mn_{0.74}Al_{0.19}Si_{1.03}O_4}$								
mixed phase I	15.4	17.7	39.7	0.1	19.6	0.1	0.3	bdl	bdl	92.9
$n = 42$		$\mathbf{Li_{3.11}Na_{0.01}Mg_{0.02}Mn_{0.84}Al_{1.05}Si_2O_8}$ (Li_2MnSiO_4 + β-eucryptite)								
mixed phase II	4.6	17.8	38.1	14.5	23.4	0.1	0.1	bdl	bdl	98.6
$n = 21$		$\mathbf{Li_{0.97}Na_{0.01}Mg_{0.01}Ca_{0.82}Mn_{1.04}Al_{1.1}Si_2O_8}$ (glaucochroite + β-eucryptite)								

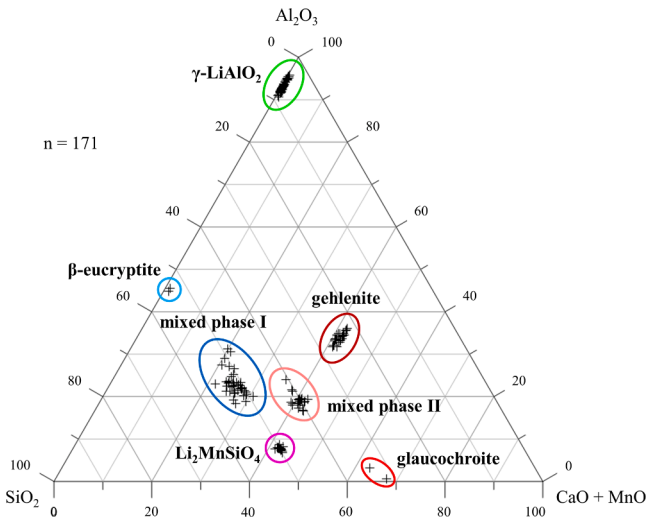

Fig. 2. Ternary diagram Al_2O_3-SiO_2-CaO + MnO illustrating the variation in the chemical composition of the slag phases measured with EPMA in wt%.

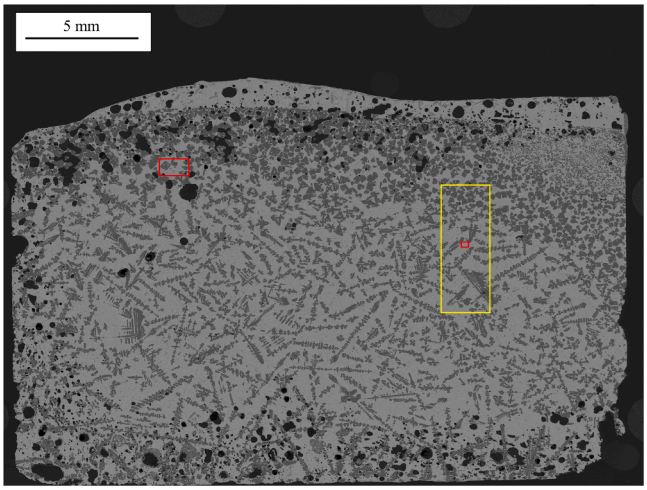

Fig. 3. BSE image of a cross section through one-half of the entire slag sample. The right side of the image shows the centre of the slag. The red rectangles mark the areas shown enlarged in Fig. 5 whereas the yellow rectangle marks the area analysed with LA-ICP-TOFMS (Figs. 6 and 7).

anhedral, appears optically homogeneous and has a grain size in the range of <1 to 50 μm. In comparison, mixed phase II is composed of very fine-grained, closely intergrown, anhedral β-eucryptite and glaucochroite. The grain size of these silicates is between <1 and 10 μm (Fig. 5b).

The modal mineralogy from the SEM-MLA examination is summarized in Table 6. The investigated area consists mainly of γ-$LiAlO_2$, gehlenite, mixed phase II, and Li_2MnSiO_4 and, to a lesser extend of mixed phase I, β-eucryptite as well as glaucochroite. The proportion of areas with unknown composition is <0.1 %.

3.2.3. LA-ICP-TOFMS

The area of the slag sample ablated by LA-ICP-TOFMS covers 451,600 pixels (5 × 5 μm each). The distribution of the element contents of Li, Al, Si, Ca, and Mn in the analysed area is shown in Fig. 6.

Median chemical composition and the spatial distribution of eight clusters determined from the cluster analysis are given in Table 7 and Fig. 7. Based on the obtained elemental composition and its similarity to the theoretical composition calculated from stoichiometry clusters 1 and 2 are assigned to gehlenite and γ-$LiAlO_2$, respectively. Cluster 3 is

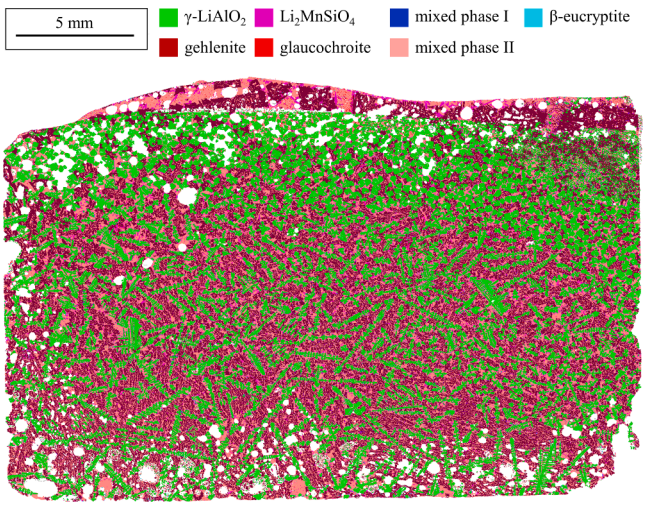

Fig. 4. Colour-coded phase distribution image of a cross section through one-half of the entire slag sample measured with SEM-based automated mineralogy (MLA). The right side of the image shows the centre of the slag.

interpreted to represent a close intergrowth of glaucochroite and β-eucryptite based on EPMA and SEM-MLA and therefore referred to as mixed phase II. Pores in the sample represented by cluster 4 are filled with epoxy resin from sample preparation. Cluster 5 mainly consists of Li, Si, and Mn and is assigned to Li_2MnSiO_4. As cluster 7 is composed of a mixture of Li_2MnSiO_4 and β-eucryptite, it is consequently assigned as mixed phase I. The spatial distributions of cluster 6 and cluster 8 reveal that these clusters mainly represent the fringes around γ-$LiAlO_2$ and gehlenite grains, respectively. Their composition corresponds approximately to a mixture of melilite, glaucochroite, and β-eucryptite or γ-$LiAlO_2$ and SiO_2 (Fig. 7).

The total chemical composition of the sample can be obtained by adding up the individual element concentrations of the different clusters in an area-weighted manner. The results are given in Table 8.

3.3. Rapid analytical methods

3.3.1. μ-EDXRF

The spatial distribution of the main elements Al, Si, Ca, and Mn in the slag sample was measured by μ-EDXRF and is shown in Fig. 8. Generally, brighter colour shades represent higher element contents, while darker colour shades indicate lower element contents. The presentation of the measured element contents as graded colours thus demonstrates differences in the mineralogical composition. The evaluation of the element distribution shows that the brighter colour in the Al distribution pattern corresponds to the target phase for Li enrichment γ-$LiAlO_2$ whereas the brighter shade in the Ca distribution as well as the darker colour in the Si distribution can be assigned to gehlenite. In contrast, the brighter shades in the Si distribution and the Mn distribution comply with Li_2MnSiO_4, glaucochroite, and β-eucryptite or Li_2MnSiO_4 and glaucochroite, respectively.

3.3.2. UVC radiation

Some of the phases present in the slag, such as β-eucryptite and γ-$LiAlO_2$, have fluorescent [9,21] and phosphorescent properties. Under certain conditions they can emit visible light of a defined wavelength when irradiated with short-wave ultraviolet radiation (254 nm). Consequently, it was investigated if the use of UVC radiation is also suitable as a rapid analysis method to visualize individual slag phases (Fig. 9). A comparison of the sample image under UVC radiation with the colour-coded phase distribution image from SEM-MLA in Fig. 4 proves that the phase with the characteristic green luminescence is the target phase γ-$LiAlO_2$.

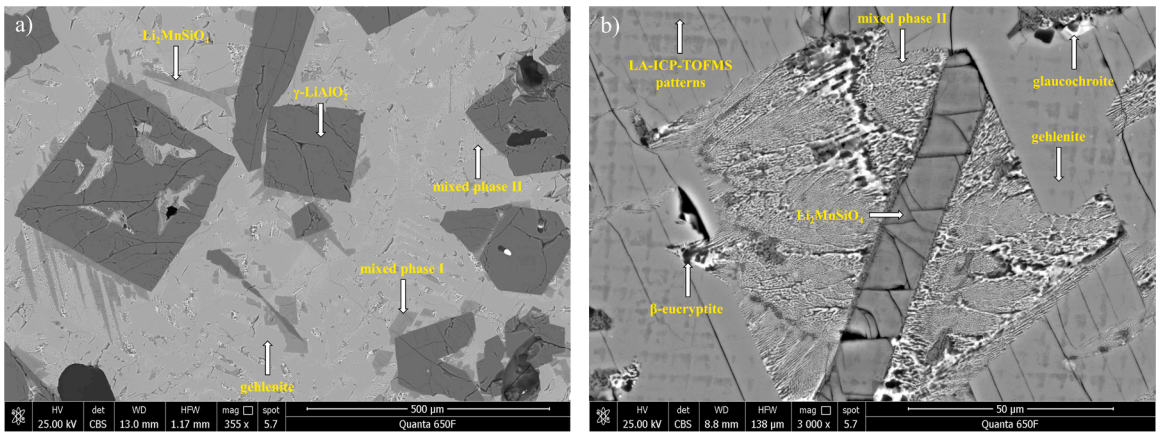

Fig. 5. BSE images of the analysed sample with the identified slag phases gehlenite, γ-$LiAlO_2$, Li_2MnSiO_4, mixed phase I, mixed phase II, glaucochroite and β-eucryptite at horizontal field widths (HFW) of a) 1.17 mm and b) 138 µm.

Table 6
Modal mineralogy of the slag sample from SEM-MLA in area %.

γ-$LiAlO_2$	gehlenite	mixed phase II	Li_2MnSiO_4	mixed phase I	β-eucryptite	glaucochroite	unknown	Total
31	31	30	4	2	1	1	< 0.1	100

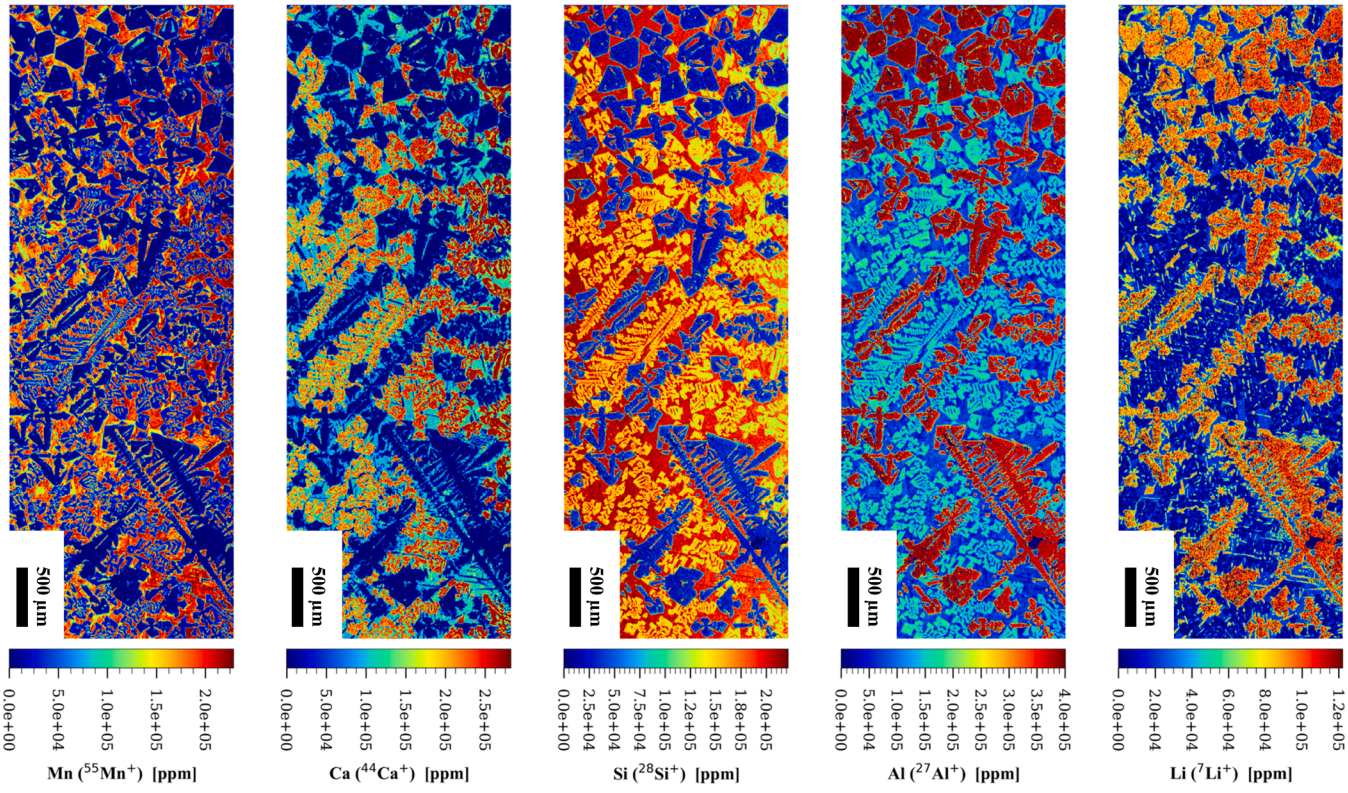

Fig. 6. Spatial distribution of the element contents of Mn, Ca, Si, Al, and Li in the area (see Fig. 3) investigated by LA-ICP-TOFMS.

4. Discussion

4.1. Chemical composition of the sample

The chemical composition of the sample was calculated from the weighed-in pure substances prior to melting (Table 2) and analysed by XRF/ICP-MS and LA-ICP-TOFMS (Table 9). The amount of sample material ablated by LA-ICP-TOFMS is estimated to be <0.03 mg (ablated area: 11 mm^2, ablation depths: <1 µm, sample density 3 g/cm^3). Compared to the sample aliquots used for XRF/ICP-MS analysis (1000 mg and 50 mg, respectively) the amount of sample material used in LA-ICP-TOFMS is significantly smaller. Having this in mind, the results of XRF/ICP-MS should be more representative for the heterogeneous slag than those measured by LA-ICP-TOFMS. However, the results obtained by XRF/ICP-MS and LA-ICP-TOFMS agree well taking into account the variable sample volumes and the fact that a heterogeneous sample was

Table 7
Median chemical composition based on LA-ICP-TOFMS data of the eight clusters determined from the cluster analysis and calculated formulas of the slag phases.

Cluster No.	Area [Pixel]	Assigned mineralogy	Portion [area %]	Li_2O [wt %]	Al_2O_3 [wt %]	SiO_2 [wt %]	CaO [wt %]	MnO [wt %]	Na_2O [wt %]	MgO [wt %]
1	101,813	gehlenite	23	1.0	31.1	31.0	33.1	3.1	0.4	0.3
				$Ca_{1.57}Na_{0.03}Li_{0.18}Mg_{0.02}Mn_{0.12}Al_{1.63}Si_{1.37}O_7$						
2	119,521	γ-$LiAlO_2$	27	21.0	70.4	6.8	0.0	0.9	0.4	0.1
				$Li_{0.93}Na_{0.01}Mn_{0.01}Al_{0.91}Si_{0.08}O_2$						
3	104,427	mixed phase II	24	4.5	13.0	41.9	15.7	24.3	0.8	0.3
				$Li_{0.94}Na_{0.08}Ca_{0.87}Mg_{0.02}Mn_{1.06}Al_{0.79}Si_{2.17}O_8$ (glaucochroite + β-eucryptite)						
4	12,850	Resin								
5	27,375	Li_2MnSiO_4	6	15.6	9.6	44.7	3.3	25.8	1.6	0.5
				$Li_{1.52}Na_{0.08}Ca_{0.09}Mg_{0.02}Mn_{0.53}Al_{0.27}Si_{1.08}O_4$						
6	23,733	fringe area of γ-$LiAlO_2$	5	19.1	50.6	18.6	2.0	5.3	1.1	0.2
				$Li_{0.89}Na_{0.03}Ca_{0.03}Mn_{0.05}Al_{0.69}Si_{0.22}O_2$						
7	33,038	mixed phase I	8	16.0	19.7	42.4	2.7	17.4	1.3	0.4
				$Li_3Na_{0.12}Ca_{0.14}Mg_{0.03}Mn_{0.69}Al_{1.09}Si_{1.98}O_8$ (Li_2MnSiO_4 + β-eucryptite)						
8	28,843	fringe area of gehlenite	7	2.8	22.2	37.7	24.0	12.0	1.1	0.4
				$Li_{1.07}Na_{0.2}Ca_{2.44}Mg_{0.06}Mn_{0.97}Al_{2.49}Si_{3.58}O_{15}$ (melilite + glaucochroite + β-eucryptite)						

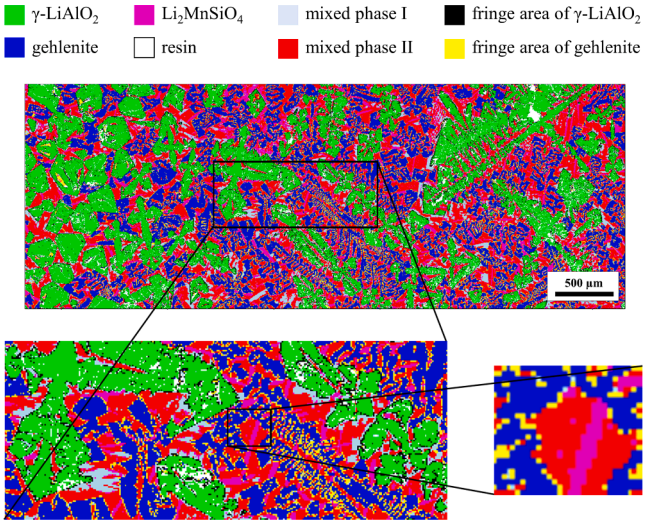

Fig. 7. Spatial distribution (area is indicated in Fig. 3) of the slag phases derived from the eight clusters determined from the cluster analysis of LA-ICP-TOFMS data. The small rectangle marks the area shown enlarged in Fig. 5b.

Table 8
Total sample composition obtained by LA-ICP-TOFMS in wt%.

Li_2O	Al_2O_3	SiO_2	CaO	MnO	Na_2O	MgO	Total
10.4	35.8	28.5	13.5	10.8	0.7	0.3	100

analysed (Table 9). A comparison of the XRF/ICP-MS results with the weighed-in composition before melting shows that in addition to the weighed-in contents of Al_2O_3, SiO_2, CaO, MnO, and Li_2O minor concentrations of MgO and Na_2O were detected. The presence of the latter oxides is probably a result of a slight contamination of the starting materials. Furthermore, a significant depletion of about 16 % was detected for Li_2O, which indicates that during the melting process Li gets lost. The loss of Li during the production of the slags has already been observed by [52] and must be taken into account to increase the recovery rate of Li in LIBs recycling via a combined pyro- and hydrometallurgical process.

4.2. Mineralogical composition of the sample

4.2.1. Phase composition

The phase composition of the sample was quantified by XRD (Rietveld method), SEM-MLA, and LA-ICP-TOFMS. Each method uses a different approach for quantifying the phase composition. XRD was performed on a powder sample taken from a ground and homogenized part of a half of the sample. The Rietveld method uses crystallographic data of the whole sample to quantitatively determine the crystalline phases present in the sample and to determine the non-crystalline (amorphous) portion of the sample. SEM-MLA and LA-ICP-TOFMS measurements were carried out on a polished cross section of the slag and use spatially resolved material properties and element concentration data from which the quantitative phase composition of the sample is deduced. SEM-MLA was applied on the entire polished sample cross section while LA-ICP-TOFMS was applied on a selected subarea of approximately 11 mm^2 due to data volume and analysis time constraints.

The results of the different investigation methods are given in Tables 4, 6, and 7 and show significant differences in both the qualitative and quantitative phase compositions. Rietveld analysis identifies substantial portions of glaucochroite, β-eucryptite, and an amorphous phase, which does not appear in the evaluation of the SEM-MLA and LA-ICP-TOFMS data. On the other hand, SEM-MLA and LA-ICP-TOFMS identify two mixed phases and LA-ICP-TOFMS additionally identifies fringe areas on γ-$LiAlO_2$ and gehlenite. These differences in the data are primarily caused by small grain sizes and close intergrowths of different phases, which cannot be spatially resolved by LA-ICP-TOFMS (and in some cases also not by SEM-MLA), and the fact that the amorphous portion of the sample can be quantified by Rietveld analysis, but its composition cannot be determined by this method directly. The discussion below shows how the apparently contradictory results can be reconciled.

Fig. 7 illustrates that the fringe areas detected by LA-ICP-TOFMS are almost always located at the boundaries between gehlenite and mixed phase II or between γ-$LiAlO_2$ and mixed phase II. Furthermore, the two fringe areas are only one pixel wide. When the 5 µm square laser spot hits the contact between two phases, both phases are ablated and an analytical result is obtained from a mixture of both phases. The results for all laser spots located on the phase boundary between gehlenite and mixed phase II show similar geochemical analyses. The same applies to the phase boundary between γ-$LiAlO_2$ and mixed phase II. The two different phase boundaries have different geochemical signatures and are identified as two different clusters by cluster analysis. As these analyses on the two-phase boundaries do not represent separate phases, but are each the result of a mixture of the phases involved, the area

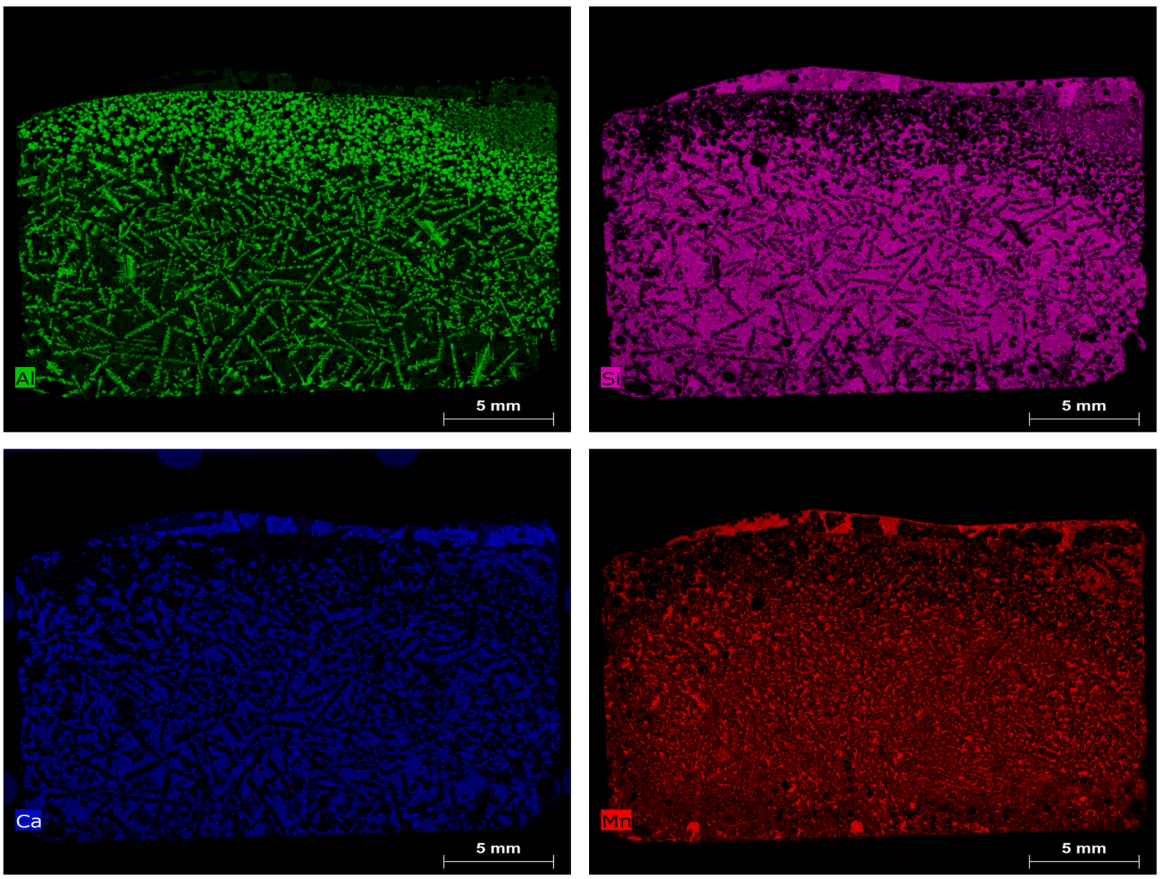

Fig. 8. Distribution of the element contents of Al, Si, Ca, and Mn from the investigation of a cross section through one-half of the entire slag sample with μ-EDXRF.

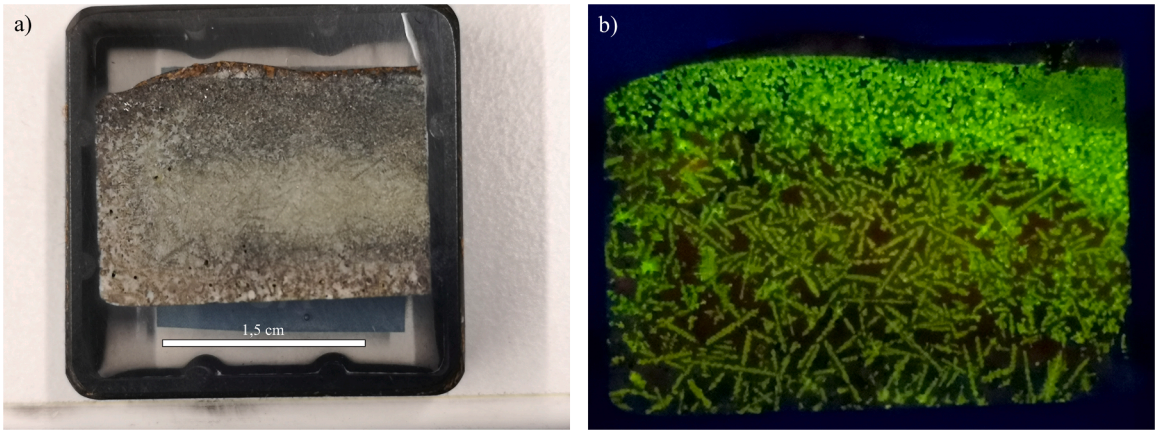

Fig. 9. a) Photo of the sample and b) photo of the sample under short-wave ultraviolet radiation (254 nm).

Table 9
Comparison of total sample composition before melting and analysed after melting by XRF/ICP-MS and LA-ICP-TOFMS in wt%.

	Li_2O	Al_2O_3	SiO_2	CaO	MnO	Na_2O	MgO
weighed-in before melting	11.5	37.5	25.0	15.9	10.1	-	-
XRF/ICP-MS	9.7	38.8	24.6	16.4	10.2	0.02	0.16
LA-ICP-TOFMS	10.4	35.8	28.5	13.5	10.8	0.7	0.3

proportions of these analyses can, as a first approximation, be attributed equally to the two phases involved.

Since Rietveld analysis reports phase fractions in wt% but the data from SEM-MLA and LA-ICP-TOFMS are given in area %, the latter are converted into wt% by using the different densities of the phases involved. For the two mixed phases, the respective density was estimated from the theoretical composition given in Table 7. The following densities (g/cm³) were used: γ-$LiAlO_2$ (2.62), gehlenite (3.04), glaucochroite (3.48), β-eucryptite (2.66), Li_2MnSiO_4 (2.98), mixed phase I (2.82), and mixed phase II (3.18).

If the procedures described above are applied on the data obtained with SEM-MLA and LA-ICP-TOFMS, a comparison of the quantitative phase composition of the three methods is possible and given in Table 10.

The results of SEM-MLA and LA-ICP-TOFMS are rather similar, but

they partly differ from the Rietveld analysis data. Only for γ-$LiAlO_2$ and Li_2MnSiO_4 all methods provide comparable results. Glaucochroite, β-eucryptite, and amorphous constituents could be detected by Rietveld analysis, but these phases do not appear in substantial amounts in SEM-MLA and LA-ICP-TOFMS data. Conversely, SEM-MLA and LA-ICP-TOFMS detect two mixed phases that cannot be assigned to a specific phase. Gehlenite is detected by all methods but the portion detected by XRD is somewhat lower than that detected by SEM-MLA and LA-ICP-TOFMS.

The main point to explain the differences between the three methods is the question how the amorphous fraction and the portions of glaucochroite and β-eucryptite, as detected by Rietveld analysis, are reflected in the data from SEM-MLA and LA-ICP-TOFMS. All three methods result in approximately equal proportions for γ-$LiAlO_2$ and Li_2MnSiO_4, which indicates that these phases are essentially crystalline, because XRD only detects crystalline phases. Glaucochroite and β-eucryptite, which were quantified in Rietveld analysis, sum up to 19 wt%, but were not detected by LA-ICP-TOFMS. These phases are very fine-grained and closely intergrown. A comparison of Fig. 5b with the area in the small rectangle in Fig. 7 show that the 5 μm spot size of the LA-ICP-TOFMS is not sufficient to measure them individually. Consequently, glaucochroite and β-eucryptite are always recorded as mixed analysis and included in mixed phase II of the LA-ICP-TOFMS data. However, the portion of mixed phase II reported by SEM-MLA and LA-ICP-TOFMS is 32 wt%, which is substantial larger than the sum of glaucochroite and β-eucryptite (19 wt%). The remaining difference is attributed to an amorphous portion of 13 wt% of the residual melt, indicating that mixed phase II contains both crystalline and amorphous components. If this 13 wt% of amorphous portion are subtracted from the 28 wt% of total amorphous portion determined by Rietveld analysis, then 15 wt% of amorphous constituents remains. Due to the fact that the portion of gehlenite obtained by Rietveld analysis is about 10 wt% lower than the portion given by SEM-MLA and LA-ICP-TOFMS, about one-third-of the residual melt seems to have gehlenite composition and is part of the amorphous phase. The remaining 5 wt% of the total amorphous amount is attributed to mixed phase I of SEM-MLA and LA-ICP-TOFMS data, as this phase could not be detected by XRD.

As a result, it is deduced that: a) γ-$LiAlO_2$ and Li_2MnSiO_4 are crystalline, b) gehlenite and mixed phase II seem to contain amorphous portions, c) the crystalline glaucochroite and β-eucryptite are part of mixed phase II and d) mixed phase I is amorphous.

4.2.2. Chemical composition of the slag phases

The quantitative chemical compositions of the slag phases were measured using EPMA and LA-ICP-TOFMS. Both methods use fundamentally different approaches to determine the chemical composition. The results from EPMA are based on quantified point analyses (given as average values of selected analyses in Table 5), whereas the results of the LA-ICP-TOFMS (Table 7) are based on median values of tens of thousands 5 μm square pixel measurements. As the laser spot of the LA-ICP-TOFMS is larger than the smallest grain size present, the data set also includes numerous mixed analyses. Accordingly, the EPMA analyses should be more representative, even if the Li_2O content must be estimated from the deficit in the mass balance and the stoichiometry of the respective slag phase. Overall, the results obtained by EPMA and LA-ICP-TOFMS agree well. The chemical composition of gehlenite ($Ca_2Al_2SiO_7$), glaucochroite ($CaMnSiO_4$), and β-eucryptite ($LiAlSiO_4$) measured by EPMA largely corresponds to the theoretical stoichiometric composition. However, glaucochroite and β-eucryptite could only be measured twice each due to the small grain size and the close intergrowth of these phases. They were mainly recorded as mixed phase II, which has a chemical composition corresponding to a mixture of glaucochroite and β-eucryptite in a ratio of approximately 1 to 1 ($Ca_{0.82}Mg_{0.01}Mn_{1.04}SiO_4$ + $Li_{0.97}Na_{0.01}Al_{1.1}SiO_4$). Noteworthy are the observed small quantities of Si in γ-$LiAlO_2$, which were measured with both EPMA and LA-ICP-TOFMS. They confirm the incorporation of Si into the γ-$LiAlO_2$ structure following the coupled substitution $Li^+ + Al^{3+} = Si^{4+} + \square$ (vacancy) described by [20]. The EPMA results show that γ-$LiAlO_2$ contains between 1.40 and 3.17 wt% Si. These contents correspond to around 0.03 and 0.08 atoms per formula unit (apfu), respectively. The exchange reaction reduces the Li content of γ-$LiAlO_2$ and leads to variable solid solutions with the general formula $Li_{1-x}Al_{1-x}Si_xO_2$. The EPMA results further show that the slag phase designated as Li_2MnSiO_4 contains besides Li, Mn, and Si also 2.85 to 3.45 wt% Al (0.17 to 0.21 apfu). The calculated formulas from EPMA ($Li_{1.81}Na_{0.01}Ca_{0.01}Mg_{0.02}Mn_{0.74}Al_{0.19}Si_{1.03}O_4$) as well as from LA-ICP-TOFMS ($Li_{1.52}Na_{0.08}Ca_{0.09}Mg_{0.02}Mn_{0.53}Al_{0.27}Si_{1.08}O_4$) indicate that this phase could be a Li_2MnSiO_4-rich solid solution of the poorly investigated solid solution series Li_2MnSiO_4 – β-eucryptite. The general formula for this compound can be given as $Li_{2-x}Mn_{1-x}Al_xSiO_4$. Mixed phase I consists like Li_2MnSiO_4 mainly of Li, Al, Si, and Mn. Formula calculations based on the arithmetic average of the EPMA measurements reveal that this phase is also composed of a mixture of Li_2MnSiO_4 and β-eucryptite, but in a ratio of nearly 1 to 1 ($Li_{2.06}Mn_{0.86}Mg_{0.02}SiO_4$ + $Li_{1.05}Na_{0.01}Al_{1.05}SiO_4$). The fringe areas of gehlenite and γ-$LiAlO_2$ measured with LA-ICP-TOFMS are chemically composed of Li, Al, Ca, Si, and Mn and Li, Al, Si, and Mn, respectively. The median chemical composition of the fringe area of gehlenite is close to a mixture of equal proportions of melilite, glaucochroite and β-eucryptite (($Ca_{1.44}Na_{0.2}$)$_{1.64}$($Mg_{0.06}Al_{1.49}Si_{1.58}$)$_{3.13}O_7$ + $CaMn_{0.97}SiO_4$ + $Li_{1.07}AlSiO_4$), while the composition of the fringe area of γ-$LiAlO_2$ corresponds rather to a Si-bearing γ-$LiAlO_2$ ($Li_{1-x}Al_{1-x}Si_xO_2$) with minor proportions of glaucochroite.

4.2.3. Chemical composition of the amorphous slag phases

The chemical composition of the amorphous constituents was calculated as the difference between the chemical composition of the quantitative, crystalline phase constituents and the total chemistry. Quantitative phase composition from the Rietveld analysis was used to obtain the portions of the different crystalline phases present in the slag sample (Table 4), the chemical composition of those phases was obtained from EPMA (Table 5), and the total chemical composition of the slag sample was obtained from XRF/ICP-MS (Table 3). The results of the calculations are shown in Table 11.

4.2.4. Allocation of Li and Mn in the slag phases

In addition to calculating the chemical composition of the amorphous components, the distribution of Li and Mn in the slag phases can be calculated from the results of the Rietveld analysis, EPMA, and XRF/ICP-MS to enhance the thermodynamic database and for process control.

Table 10
Comparison of the quantitative phase composition in wt% obtained by XRD after Rietveld refinement, SEM-MLA, and LA-ICP-TOFMS.

	XRD (Rietveld)	SEM-MLA	LA-ICP-TOFMS
γ-$LiAlO_2$	29	28	27
gehlenite	20	32	27
glaucochroite	12	1	-
β-eucryptite	7	1	-
Li_2MnSiO_4	4	4	6
mixed phase I (Li_2MnSiO_4 + β-eucryptite)	-	2	7
mixed phase II (glaucochroite + β-eucryptite)	-	32	32
amorphous	28	-	-

Table 11
Calculated chemical composition of the amorphous constituents in wt%.

Li_2O	Al_2O_3	SiO_2	CaO	MnO	MgO	Total
7	28	32	18	14	<1	100

The results are presented in Fig. 10. According to the calculation about 80 % of the Li_2O and approximately 61 % of the MnO content of the sample is bound in the crystalline slag phases.

4.2.5. Microstructure

The microstructure of the sample was examined using SEM, SEM-MLA and LA-ICP-TOFMS. The results demonstrate that a combination of SEM and SEM-MLA is more suitable for analysing the microstructure of the slag, as the spatial resolution of the LA-ICP-TOFMS is significantly lower than the smallest grain size present (Fig. 5b and 7). Nevertheless, the obtained results of both approaches illustrate very well the heterogeneous composition of the sample. The grain size of the slag phases is in a range between < 1 μm to 5 mm. In the upper part of the sample, which has cooled down the fastest, a rim mainly composed of skeletal gehlenite, euhedral Li_2MnSiO_4, and mixed phase II has formed. Below this rim, euhedral to dendritic crystals of γ-$LiAlO_2$ and gehlenite as well as euhedral crystals of Li_2MnSiO_4 are present in a silicate groundmass of mixed phases I and II. The amorphous constituents cannot be determined by SEM-MLA or LA-ICP-TOFMS. As discussed in Section 4.2.1 it is assumed that mixed phase I as well as parts of mixed phase II are amorphous. The same holds true for residual melt with gehlenite composition. The occurrence of large euhedral γ-$LiAlO_2$ crystals in the upper part of the sample (Fig. 4) indicates a density separation during cooling of the melt. Since γ-$LiAlO_2$ has the lowest density (2.62 g/cm^3) of all identified slag phases, future studies should investigate whether this property can be used to pre-enrich γ-$LiAlO_2$ in the pyrometallurgical process step. Based on the crystal shape, distribution, grain size, and degree of intergrowth of the slag phases, the following crystallization sequence can be derived from the microstructure analysis: γ-$LiAlO_2$, gehlenite, Li_2MnSiO_4, β-eucryptite/glaucochroite. The crystallization sequence is the same for all slag compositions considered in the PyroLith project and corresponds largely to the crystallization sequence simulated for various slag compositions in the Al_2O_3–SiO_2–CaO–MnO–Li_2O system with an optimized thermodynamic model [23].

4.3. Rapid analytical methods

In addition to the established analysis methods, two rapid methods for in-process slag analysis were tested: μ-EDXRF and UVC radiation. The spatial distribution of Al, Si, Ca, and Mn was mapped using μ-EDXRF on a cross section through one-half of the entire slag sample. The presentation of the measured individual element contents as graded colours enables the identification of areas with different element contents, which reflect variations in mineralogy. Since the phases occurring in the compositional range of the Al_2O_3–SiO_2–CaO–MnO–Li_2O system relevant for LIBs recycling are largely known, the distribution patterns of the element contents can be clearly assigned to individual slag phases. This can be shown by a comparison of the element distribution patterns (Fig. 8) with the colour-coded phase distribution image from the SEM-MLA (Fig. 4). Here the brighter colour in the Al distribution pattern corresponds to γ-$LiAlO_2$. The brighter shade in the Ca distribution pattern as well as the darker colour in the Si distribution pattern can be assigned to gehlenite. Due to the relatively low spatial resolution of the method of 20 μm, Li_2MnSiO_4 and the fine-grained, closely intergrown matrix phases glaucochroite and β-eucryptite cannot be discriminated. They were recorded as a mixed analysis in the bright colour of the Si distribution pattern and in the Mn distribution pattern. For further evaluation, the individual element patterns can be combined to a colour-coded element distribution image that is comparable to the colour-coded phase distribution image from the SEM-MLA examination (Fig. 11). The combined element distribution image generated from μ-EDXRF data has a lower resolution, but is quickly available and can be used for preliminary microstructure analyses.

UVC radiation was used to visualise slag phases with fluorescent or phosphorescent properties in the examined sample. Irradiating the sample with short-wave UV radiation has shown that only one slag phase gives a characteristic green luminescence and pronounced phosphorescence. The observed luminescence could be assigned to γ-$LiAlO_2$ by comparison of the image taken under UVC radiation (Fig. 9b) with the colour-coded phase distribution image from SEM-MLA (Fig. 4). In order to investigate whether the luminescence of γ-$LiAlO_2$ is caused by an

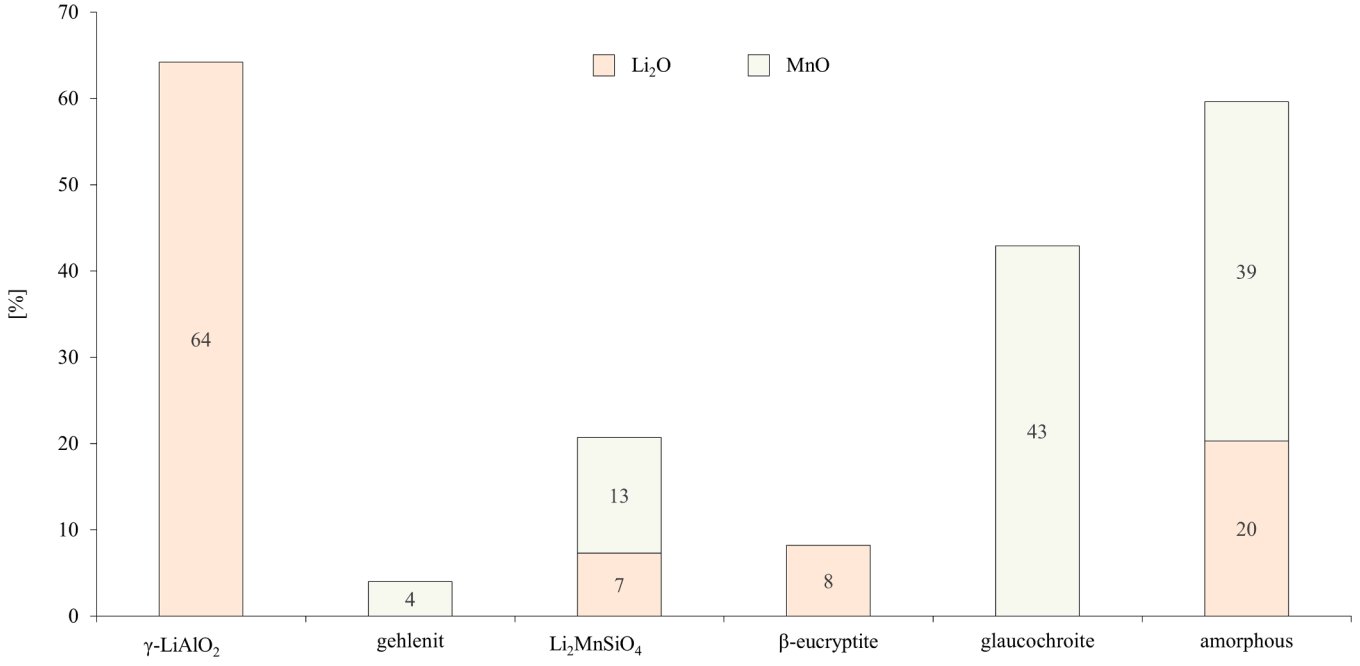

Fig. 10. Allocation of Li_2O and MnO in the detected slag phases.

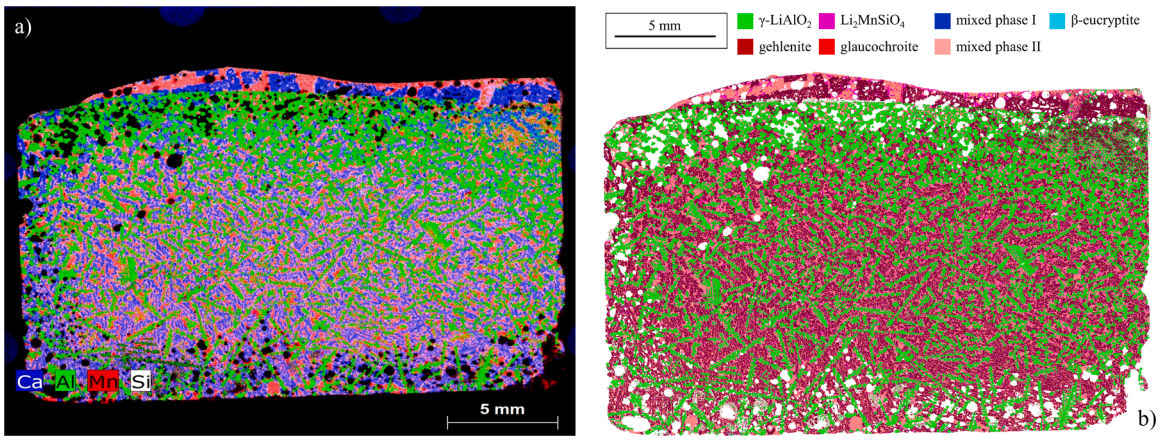

Fig. 11. Comparison of (a) the combined element distribution image from μ-EDXRF with (b) the colour- coded phase distribution image from the examination of the sample with SEM-MLA.

activator ion or crystal structure defects, further investigations were carried out using CL microscopy with spectrally resolved detection of the related emission bands (spectral CL). In contrast to short-wave UV radiation, luminescence in CL is excited by an electron beam. The findings of the spectral CL are depicted in Fig. 12.

The results reveal that γ-$LiAlO_2$ exhibits a stable green CL colour. The emission spectrum is dominated by a sharp emission band with a maximum at approximately 540 nm. These observations indicate that the green CL of γ-$LiAlO_2$ is caused by Mn^{2+} [4,15,16]. This finding is supported by the EPMA results (Table 5) as well as by further investigations carried out in the frame of the PyroLith project. These investigations prove that γ-$LiAlO_2$ exhibits no luminescence in samples with 0.6 wt% MnO, while an increase in the intensity of the luminescence was observed in samples with increasing MnO contents (2 wt% to 4.5 wt%) (Figure S1 in the Electronic Supplementary Material). The phosphorescent properties of γ-$LiAlO_2$ can therefore be attributed to a doping with Mn^{2+}. It strongly depends on the MnO content of the slag and thus on the concentration of the dopant in the crystal.

The evaluation of the results reveals that both rapid analytical methods are suitable to assess the relative content, grain size, crystal shape and the spatial distribution of the main slag phases within a few seconds (UVC radiation) or a few hours (μ-EDXRF). The main advantage of both rapid analytical methods over conventional techniques is their minimal sample preparation requirements. For μ-EDXRF analysis, a flat sample surface is sufficient. The method can be applied directly to sawn or polished samples, and the data processing effort is minimal. Element distribution maps are available almost immediately after measurement and can be evaluated without additional computational steps. UVC-based investigations can be performed on broken, sawn, polished, or coarsely ground samples. When irradiated with UVC light, fluorescent or phosphorescent slag phases become immediately visible, enabling the evaluation of their relative content, spatial distribution, grain size, and morphology either in real time or later through photographic documentation.

4.4. Analytical approach for the chemical and mineralogical characterization of LIB slags

Based on the presented results, the two-stage routine method illustrated in Fig. 13 is proposed for the chemical-mineralogical characterization of Al_2O_3–SiO_2–CaO–MnO–Li_2O type LIB slags. Stage 1 includes μ-EDXRF and UVC radiation, two rapid analysis methods that can be used for in-process analyses during the industrial recycling process. With μ-EDXRF the chemical composition of the sample (without Li) can be measured spatially resolved within a few hours on sawn or polished sample sections with dimensions of up to 16 cm × 20 cm. The presentation of the measured individual element contents of Al, Si, Ca, and Mn as colours gradients in element distribution images highlights differences in the mineralogical composition. Because the phases occurring in the slag system Al_2O_3–SiO_2–CaO–MnO–Li_2O and their stoichiometric compositions are largely known, the relative content, distribution, grain size, and crystal shape (euhedral, skeletal, dendritic) of the main slag phases (gehlenite, γ-$LiAlO_2$) can be assessed from the element distribution images if the grain size is appropriate

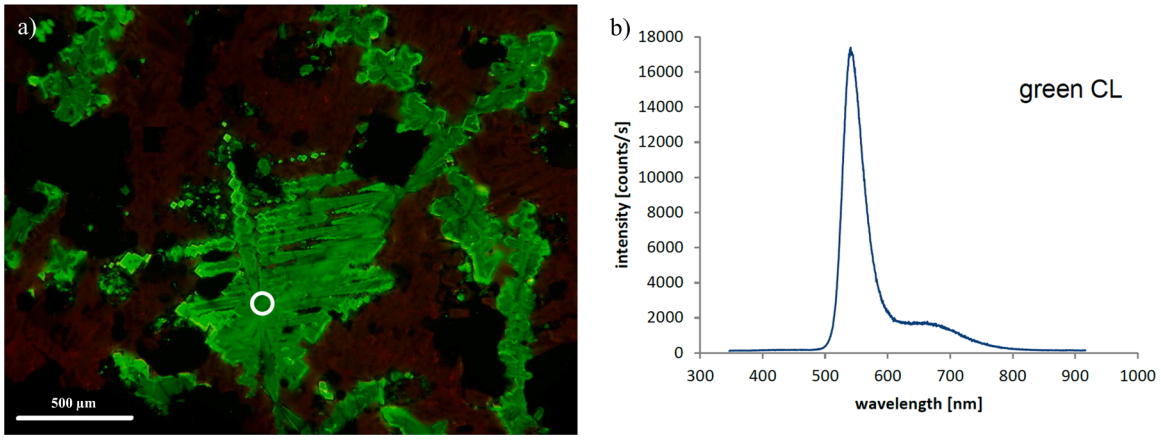

Fig. 12. a) Cathodoluminescence image and b) emission spectrum between 370 and 900 nm of dendritic γ-$LiAlO_2$. The white circle marks the area in which the measurement was carried out.

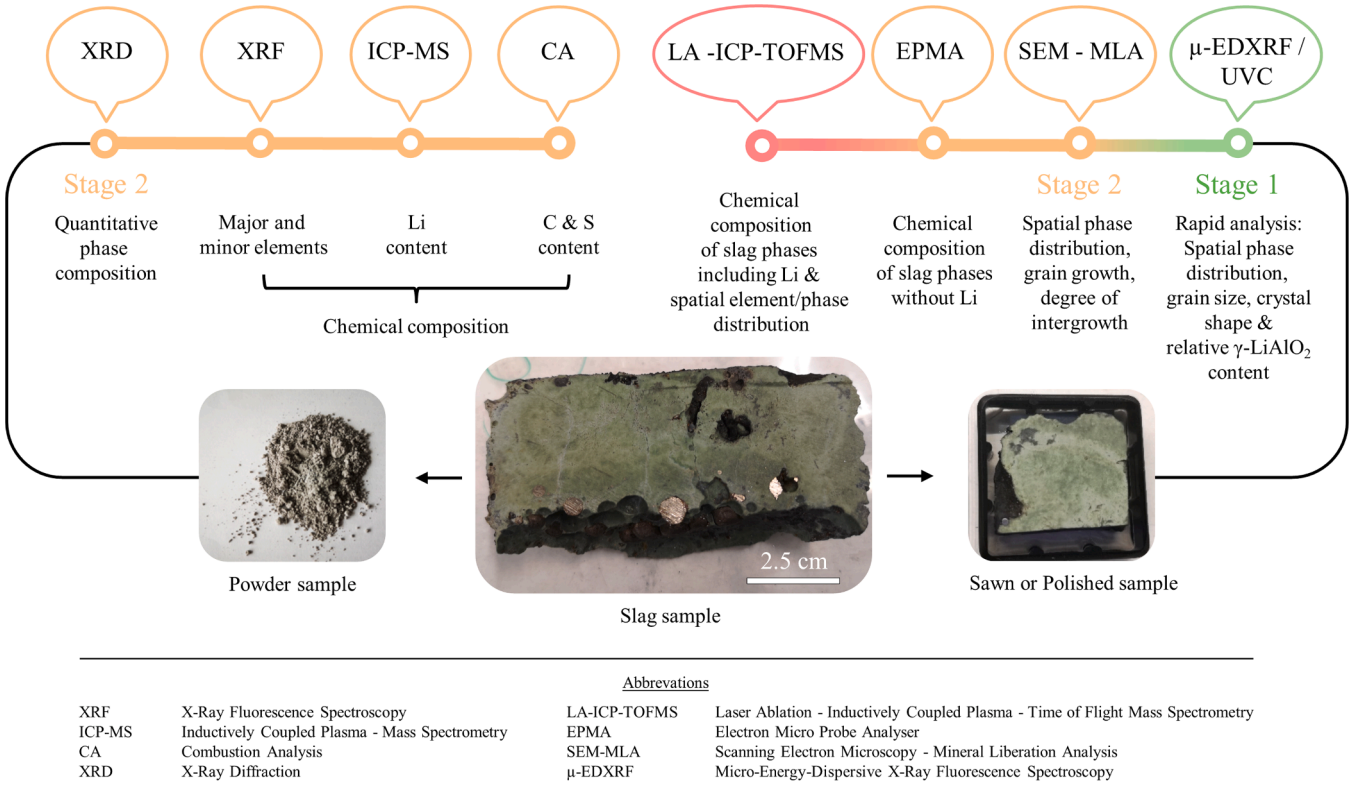

Abbrevations

XRF	X-Ray Fluorescence Spectroscopy	LA-ICP-TOFMS	Laser Ablation - Inductively Coupled Plasma - Time of Flight Mass Spectrometry
ICP-MS	Inductively Coupled Plasma - Mass Spectrometry	EPMA	Electron Micro Probe Analyser
CA	Combustion Analysis	SEM-MLA	Scanning Electron Microscopy - Mineral Liberation Analysis
XRD	X-Ray Diffraction	µ-EDXRF	Micro-Energy-Dispersive X-Ray Fluorescence Spectroscopy

Fig. 13. Routine method for the chemical-mineralogical characterization of Al_2O_3–SiO_2–CaO–MnO–Li_2O-type slags from the recycling of LIBs via a combined pyro- and hydrometallurgical process route.

(>20 µm). The combination of the element content distribution patterns results in a colour-coded image that is comparable to a SEM-MLA measurement image. In addition to µ-EDXRF, analysing the slag samples with UVC radiation (254 nm) has proven its worth. γ-$LiAlO_2$ shows a characteristic green luminescence with pronounced phosphorescence in Mn-rich slags (MnO ≥2 wt%) under short-wave UVC radiation. It is demonstrated for the first time that this property can be used to visualise the target phase of the Li enrichment process, γ-$LiAlO_2$, in a cost-efficient manner and within a few seconds, even in broken, sawn, polished, or coarsely ground samples. If the grain size is appropriate (>50 µm), the method can be utilised on large slag samples to assess the relative content, distribution, grain size, and crystal shape.

For the detailed analysis methods in stage 2, powder samples or polished sample sections are required, which increases the preparation and time expenditure significantly. Polished sample sections can be used to analyse the microstructure of the slags (phase distribution, crystal size, crystal shape, degree of intergrowth) using SEM and SEM-MLA. From the results the crystallization sequence can be derived. Polished sample sections can also be utilised to measure the quantitative chemical composition of the slag phases by EPMA. The measured chemical compositions can then be used to calculate the formulas of the solid solutions. The Li_2O content required for the calculations can be estimated from the deficit in the mass balance and the known stoichiometric composition of the respective phase. For the analysis of the bulk chemical composition of the samples as well as for the determination of its qualitative and quantitative phase composition, fine-grained powder samples are required. Any alloy components commonly present in real battery slags in form of melt droplets (containing Cu, Co, Ni, Fe) must be carefully separated by crushing, sieving, density separation, and/or magnetic separation. If the proportion of these metals in the samples is too high (>0.5 wt%), they form an alloy with the platinum crucible of the automatic melt furnace during the production of glass beads for XRF and destroy it irreparably. The content of metals in the processed samples can be checked in advance using a handheld XRF analyser. When their concentration is below 0.5 wt %, the main and minor elements can be measured by XRF and the Li content can be determined by ICP-MS after full digestion. In contrast to slags from the model system, real battery slags may also contain significant amounts of carbon and sulphur. Both elements can be quantitatively measured by a combustion analysis (CA). The qualitative and quantitative phase composition of the slag samples can be determined using XRD and Rietveld analysis. Amorphous constituents, which occurred in all synthetic and real battery slags analysed in the PyroLith project with >0.6 wt % MnO, can be quantified using an internal standard. As a reference material for determining the amorphous constituents, rutile is better suited than corundum, as the addition of corundum to the slag samples can lead to significant reflection overlaps (Figure S2 in the Electronic Supplementary Material). In the analysed sample, a total of five crystalline slag phases were identified and quantified in addition to amorphous components: γ-$LiAlO_2$, gehlenite, β-eucryptite, glaucochroite, and Li_2MnSiO_4. In real battery slags, graphite, F-containing compounds like cuspidine as well as fluorite and, in Al_2O_3-rich samples, $Li_xMn_{1-2x}Al_{2+x}O_4$ ($0 \leq x \leq 0.5$) [23] can also occur. Using the quantitative mineralogical composition from the Rietveld analysis, the total chemical composition from XRF/ICP-MS and the chemical composition of the slag phases from EPMA, the chemical composition of the amorphous constituents, and the allocation of Li and Mn can be calculated. In special cases where the distribution of Li in a sample needs to be analysed or the quantitative chemical composition of the slag phases including Li needs to be measured directly, LA-ICP-TOFMS can be used to generate a quantified element distribution map with a spatial resolution of 5 µm for smaller sections of the slag sample. Areas with similar chemical composition can then be identified by a cluster analysis. The resulting data on the quantitative chemical composition and spatial distribution of the clusters can be used to validate the modal mineralogical composition (SEM-MLA) and the quantitative chemical composition of the slag phases (EPMA).

4.5. Integration of the methods into the pyro- and hydrometallurgical recycling route for LIBs

The three main fields of application of the above slag investigation approach cover the development of process routes for LIBs recycling including pyrometallurgical treatment, the industrial process control, and the adaptation of the process routes taking into account significant changes in any of the input parameters.

A significant benchmark in the technological advancement of recycling Li from spent LIBs via slag is the successful enrichment of Li in one target phase. For this purpose, the slag has to be designed to optimize crystallization of the carrier minerals hosting the target elements and gangue mineral composition. To predict the equilibrium solidification process of the slag a thermodynamic model and a comprehensive database of the respective system composition is essential. Consequently, a comprehensive analytical data set is needed for process development including major and minor element chemical composition of the input materials and slags, as well as mineralogical and microstructure analyses of the slag phases (stage 2 of analytical approach). Whether highly sophisticated methods like the EPMA or the LA-ICP-TOFMS are really necessary in a special case, must be decided in each individual case.

The industrial process route for Li recovery during LIBs recycling via high-temperature pyrometallurgy, beneficiation, and hydrometallurgical treatment requires a number of process steps. However, the mineralogical key questions to evaluate the performance of the pyrometallurgical process cover (i) the degree of success of a pre-enrichment of the target phase γ-$LiAlO_2$ during the smelting process, (ii) the distribution characteristics of this phase in the produced slag cylinder, and (iii) the size and shape characteristics of the carrier mineral in the slag. These three questions can be quickly and cost-efficiently addressed by using the developed rapid analysis methods. For the beneficiation process of the slag important mineralogical points cover its phase composition and microstructure. Automated mineralogy (e.g. using SEM-MLA) on selected samples from crushed material provides most of these required process-mineralogical parameters (e.g. particle and grain properties, mineral liberation). For the hydrometallurgical process important mineralogical points include the concentration of Si in both, the concentrates for leaching and the Li carrier mineral γ-$LiAlO_2$. Excessive Si concentration in the leachate can lead to pipe blockages by silica gel [7], whereas high Si concentrations in the γ-$LiAlO_2$ hamper maximum recovery of Li from the process. Automated mineralogy (SEM-MLA) of the concentrates for leaching provides most of the required data, supplemented by semi-quantitative SEM-measurements for Si in γ-$LiAlO_2$.

The necessity to adapt an existing process may be caused by changes in any of the input parameters (e.g. by technological development of LIBs with strongly modified chemical composition). In such cases the thermodynamic model for the equilibrium solidification process of the slag and the used robust database of the respective system composition needs to be updated. The Rietveld analysis of the phase composition of a slag produced using the modified input material will provide robust indications for the mineralogical composition of the new slag. These data may be supplemented by information from other geochemical and mineralogical methods if necessary.

5. Summary

In order to achieve the targets of the new EU battery regulation 2023/1542, a sustainable process for the recovery of Li from slags produced during the recycling of LIBs via a combined pyro- and hydrometallurgical process route needs to be developed. One promising method is the so-called Engineering of Artificial Minerals (EnAM) strategy. The aim of this concept in battery recycling is to transfer the total Li content of the melt into the Li-rich phase γ-$LiAlO_2$ by optimizing the chemical composition. After mechanical processing of the slag and froth flotation, Li can be recovered comparatively easily from γ-$LiAlO_2$ by leaching and precipitation. This approach requires extensive chemical and mineralogical analyses of the process samples along the entire process chain.

This publication presents a new analytical approach for the geochemical, mineralogical, and structural investigation of Li-enriched slags produced during pyrometallurgical treatment of LIBs. The methodology was developed as part of the PyroLith project on artificial slags of the Al_2O_3–SiO_2–CaO–Li_2O–MnO system as well as NMC-type LIB slags and is demonstrated in the present study using an artificial Li- and Mn-rich slag of known chemical composition. All analytical results are successfully cross-validated for their reliability and accuracy. In addition, it is explained what kind of analytical methods are suitable for answering specific chemical and mineralogical questions in LIBs recycling via a combined pyro- and hydrometallurgical approach and how apparently contradictory analytical results can be reconciled.

Based on the obtained data, a two-stage analytical approach is proposed for the chemical-mineralogical characterization of LIB slags. The first stage requires only minor preparation efforts, whereas for stage two the preparation and time expenditure increase significantly. Since concentration of Li during the pyrometallurgical process step in the target phase γ-$LiAlO_2$ is crucial for its recovery in LIBs recycling, special focus of the method development was directed at the identification and characteristics (frequency of occurrence, distribution in slag cylinder, size, shape, chemistry, Si content) of this phase. Finally, the application possibilities of the developed process with regard to the requirements in Li recycling by means of a combined pyro- and hydrometallurgical process route are emphasized.

CRediT authorship contribution statement

Marko Ranneberg: Writing – original draft, Validation, Investigation, Data curation, Conceptualization. **Hans-Eike Gäbler:** Writing – original draft, Investigation, Data curation. **Simon Goldmann:** Writing – original draft, Validation, Investigation. **Wilhelm Nikonow:** Writing – original draft, Investigation. **Jens Götze:** Writing – original draft, Investigation. **Haojie Li:** Writing – original draft. **Michael Fischlschweiger:** Resources, Methodology. **Torsten Graupner:** Writing – original draft, Supervision, Resources, Project administration, Investigation, Funding acquisition, Conceptualization.

Declaration of competing interest

The authors declare that they have no known competing financial interests or personal relationships that could have appeared to influence the work reported in this paper.

Acknowledgements

The authors would like to thank the Federal Ministry of Education and Research (BMBF) for its financial support of the PyroLith project (grant number 03XP0336C). We would also like to thank H. Lucas from RWTH Aachen University for producing the slag sample, D. Henry and A. Heiner for sample preparation, and C. Wöhrl and D. Göricke for their analytical support with the EPMA and the μ-EDXRF.

Supplementary materials

Supplementary material associated with this article can be found, in the online version, at doi:10.1016/j.rineng.2026.110492.

Data availability

Data will be made available on request.

References

[1] M. Alipanah, A.K. Saha, E. Vahidi, H. Jin, Value recovery from spent lithium-ion batteries: a review on technologies, environmental impacts, economics, and supply chain, CTR 1 (2021) 152–184, https://doi.org/10.3934/ctr.2021008.

[2] C.W. Bale, E. Bélisle, P. Chartrand, S.A. Decterov, G. Eriksson, A.E. Gheribi, K. Hack, I.-H. Jung, Y.-B. Kang, J. Melançon, A.D. Pelton, S. Petersen, C. Robelin, J. Sangster, P. Spencer, M.-A. Van Ende, FactSage thermochemical software and databases, 2010–2016, Calphad 54 (2016) 35–53, https://doi.org/10.1016/j.calphad.2016.05.002.

[3] A.M. Bernardes, D.C.R. Espinosa, J.A.S. Tenório, Recycling of batteries: a review of current processes and technologies, J. Power. Sources. 130 (2004) 291–298, https://doi.org/10.1016/j.jpowsour.2003.12.026.

[4] G. Blasse, B.C. Grabmaier, Luminescent Materials, Springer Berlin Heidelberg, Berlin, Heidelberg, 1994, https://doi.org/10.1007/978-3-642-79017-1.

[5] N.J. Boxall, S. King, K.Y. Cheng, Y. Gumulya, W. Bruckard, A.H. Kaksonen, Urban mining of lithium-ion batteries in Australia: current state and future trends, Miner. Eng. 128 (2018) 45–55, https://doi.org/10.1016/j.mineng.2018.08.030.

[6] M. Chen, X. Ma, B. Chen, R. Arsenault, P. Karlson, N. Simon, Y. Wang, Recycling end-of-life electric vehicle lithium-ion batteries, Joule 3 (2019) 2622–2646, https://doi.org/10.1016/j.joule.2019.09.014.

[7] P. Davris, S. Stopic, E. Balomenos, D. Panias, I. Paspaliaris, B. Friedrich, Leaching of rare earth elements from eudialyte concentrate by suppressing silica gel formation, Miner. Eng. 108 (2017) 115–122, https://doi.org/10.1016/j.mineng.2016.12.011.

[8] W.K. De Jongh, X-ray fluorescence analysis applying theoretical matrix corrections. Stainless steel, X-Ray Spectrom. 2 (1973) 151–158, https://doi.org/10.1002/xrs.1300020404.

[9] B. Dhabekar, E.A. Raja, S. Menon, T.K. Gundu Rao, R.K. Kher, B.C. Bhatt, Identification of defect centres using TSL, PL, OSL and ESR studies in $LiAlO_2$ based phosphors, J. Phys. D: Appl. Phys. 41 (2008) 115414, https://doi.org/10.1088/0022-3727/41/11/115414.

[10] N. Doebelin, R. Kleeberg, Profex: a graphical user interface for the Rietveld refinement program BGMN, J. Appl. Crystallogr. 48 (2015) 1573–1580, https://doi.org/10.1107/S1600576715014685.

[11] J.J. Donovan, T.N. Tingle, An improved mean atomic number background correction for quantitative microanalysis, Microsc. Microanal. 2 (1996) 1–7, https://doi.org/10.1017/S1431927696210013.

[12] R. Fandrich, Y. Gu, D. Burrows, K. Moeller, Modern SEM-based mineral liberation analysis, Int. J. Miner. Process. 84 (2007) 310–320, https://doi.org/10.1016/j.minpro.2006.07.018.

[13] L. Gaines, The future of automotive lithium-ion battery recycling: charting a sustainable course, Sustain. Mater. Technol. 1–2 (2014) 2–7, https://doi.org/10.1016/j.susmat.2014.10.001.

[14] T. Georgi-Maschler, B. Friedrich, R. Weyhe, H. Heegn, M. Rutz, Development of a recycling process for Li-ion batteries, J. Power. Sources. 207 (2012) 173–182, https://doi.org/10.1016/j.jpowsour.2012.01.152.

[15] J. Götze, Kathodolumineszenz-Mikroskopie und -Spektroskopie in den geo- und Materialwissenschaften, Mitt. Österr. Miner. GES. , Mitteilungen der Österreichischen Mineralogischen Gesellschaft 147 (2002) 27–40.

[16] J. Götze, U. Kempe, Physical principles of cathodoluminescence (CL) and its applications in geosciences, in: A. Gucsik (Ed.), Cathodoluminescence and Its Application in the Planetary Sciences, Springer, Berlin, 2009, pp. 1–22.

[17] K. Govindaraju, I. Rubeska, T. Paukert, Report on Zinnwaldite ZW-C analysed by ninty-two GIT-IWG member-laboratories, Geostand. Newsl. 18 (1994) 1–42, https://doi.org/10.1111/j.1751-908X.1994.tb00502.x.

[18] Y. Gu, Automated scanning electron microscope based mineral liberation analysis an introduction to JKMRC/FEI mineral Liberation analyser, JMMCE 02 (2003) 33–41, https://doi.org/10.4236/jmmce.2003.21003.

[19] G. Harper, R. Sommerville, E. Kendrick, L. Driscoll, P. Slater, R. Stolkin, A. Walton, P. Christensen, O. Heidrich, S. Lambert, A. Abbott, K. Ryder, L. Gaines, P. Anderson, Recycling lithium-ion batteries from electric vehicles, Nature 575 (2019) 75–86, https://doi.org/10.1038/s41586-019-1682-5.

[20] B. Konar, D.-G. Kim, I.-H. Jung, Critical thermodynamic optimization of the Li2O-Al2O3-SiO2 system and its application for the thermodynamic analysis of the glass-ceramics, J. Eur. Ceram. Soc. 38 (2018) 3881–3904, https://doi.org/10.1016/j.jeurceramsoc.2018.04.031.

[21] P. Koseva, P. Tzvetkov, A. Ivanov, A. Yordanova, V. Nikolov, Rare Earth doped silicate glass-ceramics for LED application, Bulg. Chem. Commun. (2018) 173–178.

[22] G.A. Lager, E.P. Meagher, High-temperature structural study of six olivines, Am. Mineral. 63 (1978) 365–377.

[23] H. Li, H. Qiu, M. Ranneberg, H. Lucas, T. Graupner, B. Friedrich, B. Yagmurlu, D. Goldmann, J. Bremer, M. Fischlschweiger, Enhancing lithium recycling efficiency in pyrometallurgical processing through thermodynamic-based optimization and design of spent lithium-ion battery slag compositions, ACS Sustain. Resour. Manag. (2024), https://doi.org/10.1021/acssusresmgt.4c00064 acssusresmgt.4c00064.

[24] H. Li, H. Qiu, T. Schirmer, D. Goldmann, M. Fischlschweiger, Tailoring lithium aluminate phases based on thermodynamics for an increased recycling efficiency of Li-ion batteries, ACS EST Eng. 2 (2022) 1883–1895, https://doi.org/10.1021/acsestengg.2c00105.

[25] LIBRI, 2011. Entwicklung eines realisierbaren recyclingkonzeptes für die hochleistungsbatterien zukünftiger elektrofahrzeuge. Lithium-Ionen Batterierecycling Initiative - LIBRI. Abschlussbericht im rahmen des FuE-Programms “förderung von forschung und Entwicklung im Bereich der Elektromobilität.” http://www.doi.org/10.2314/GBV:727409611.

[26] H. Lukas, S.G. Fries, B. Sundman, Computational Thermodynamics: The Calphad Method, 1st ed., Cambridge University Press, 2007 https://doi.org/10.1017/CBO9780511804137.

[27] W. Lv, Z. Wang, H. Cao, Y. Sun, Y. Zhang, Z. Sun, A critical review and analysis on the recycling of spent lithium-ion batteries, ACS Sustain. Chem. Eng. 6 (2018) 1504–1521, https://doi.org/10.1021/acssuschemeng.7b03811.

[28] B. Makuza, Q. Tian, X. Guo, K. Chattopadhyay, D. Yu, Pyrometallurgical options for recycling spent lithium-ion batteries: a comprehensive review, J. Power. Sources. 491 (2021) 229622, https://doi.org/10.1016/j.jpowsour.2021.229622.

[29] M. Marezio, The crystal structure and anomalous dispersion of γ-$LiAlO_2$, Acta Cryst. 19 (1965) 396–400, https://doi.org/10.1107/S0365110X65003511.

[30] Y. Miao, P. Hynan, A. Von Jouanne, A. Yokochi, Current Li-ion battery technologies in electric vehicles and opportunities for advancements, Energies. (Basel) 12 (2019) 1074, https://doi.org/10.3390/en12061074.

[31] R.D. Neuser, F. Bruhn, J. Götze, D. Habermann, D. Richter, Kathodolumineszenz: methodik und anwendung, Zentralblatt für Geologie und Paläontologie Teil 1 (H 1/2) (1995) 287–306.

[32] W. Nikonow, D. Rammlmair, Automated mineralogy based on micro-energy-dispersive X-ray fluorescence microscopy (μ-EDXRF) applied to plutonic rock thin sections in comparison to a mineral liberation analyzer, Geosci. Instrum. Method. Data Syst. 6 (2017) 429–437, https://doi.org/10.5194/gi-6-429-2017.

[33] W. Nikonow, D. Rammlmair, J.A. Meima, M.C. Schodlok, Advanced mineral characterisation and petrographic analysis by μ-EDXRF, LIBS, HSI and hyperspectral data merging, Miner. Petrol. 113 (2019) 417–431, https://doi.org/10.1007/s00710-019-00657-z.

[34] W.W. Pillars, D.R. Peacor, The crystal structure of beta eucryptite as a function of temperature, Am. Mineral. 58 (1973) 681–690.

[35] V.V. Politaev, A.A. Petrenko, V.B. Nalbandyan, B.S. Medvedev, E.S. Shvetsova, Crystal structure, phase relations and electrochemical properties of monoclinic Li2MnSiO4, J. Solid. State Chem. 180 (2007) 1045–1050, https://doi.org/10.1016/j.jssc.2007.01.001.

[36] D.S. Premathilake, F. Colombi, A.B. Botelho Junior, J.A. Soares Tenório, D. C. Romano Espinosa, M. Vaccari, Recycling lithium-ion battery graphite: synthesis of adsorbent materials for highly efficient removal of dye and metal ions from wastewater, Results. Eng. 22 (2024) 102232, https://doi.org/10.1016/j.rineng.2024.102232.

[37] H. Qiu, H. Li, M. Fischlschweiger, M. Ranneberg, T. Graupner, S. Hellmers, A. Kwade, B. Yagmurlu, A study of the floatability and leaching behavior of eucryptite and eucryptite-containing slag, Results. Eng. 27 (2025) 105702, https://doi.org/10.1016/j.rineng.2025.105702.

[38] H. Qiu, H. Li, M. Fischlschweiger, M. Ranneberg, T. Graupner, H. Lucas, C. Stallmeister, B. Friedrich, B. Yagmurlu, D. Goldmann, Valorization of lithium containing slags from pyrometallurgical recycling route of spent lithium-ion batteries: the enrichment of γ-LiAlO2 phase from thermodynamic controlled and modified slags, Miner. Eng. 217 (2024) 108918, https://doi.org/10.1016/j.mineng.2024.108918.

[39] Quix, M., van Horebeek, D., Suetens, T., 2017. Lithium-rich metallurgical slag. Patent. WO 2020/121663 A1.

[40] C. Rachmawati, J. Weiss, H.I. Lucas, E. Löwer, T. Leißner, D. Ebert, R. Möckel, B. Friedrich, U.A. Peuker, Characterisation of the grain morphology of artificial minerals (EnAMs) in lithium slags by correlating multi-dimensional 2D and 3D methods, Minerals 14 (2024) 130, https://doi.org/10.3390/min14020130.

[41] M. Ranneberg, H. Lucas, H. Li, T. Graupner, M. Fischlschweiger, B. Friedrich, Evaluation of Li and Mn influence on Al-Ca-Si-O slag system regarding pyrometallurgical LIBs treatement, in: 8th Slag Valorisation Symposium. Presented at the 8th Slag Valorisation Symposium, Mechelen, Belgium, 2023.

[42] G. Ren, S. Xiao, M. Xie, B. Pan, F. Youqi, F. Wang, X. Xia, Recovery of valuable metals from spent lithium-ion batteries by smelting reduction process based on FeO–SiO 2 –Al 2 O 3 slag system, Trans. Nonferrous Met. Soc. China 27 (2017) 450–456, https://doi.org/10.1016/S1003-6326(17)60051-7.

[43] N. Saunders, A.P. Miodownik, CALPHAD (calculation of Phase diagrams): a Comprehensive guide, Pergamon materials Series, Pergamon, Oxford; New York, 1998.

[44] Scheunis, L., Callebaut, W., 2022. Process for the recovery of lithium. Patent. WO 2020/104164.

[45] R. Sojka, Q. Pan, L. Billmann, Comparative Study of Li-ion Battery Recycling Processes, Accurec Recycling GmbH, 2020.

[46] M. Sommerfeld, C. Vonderstein, C. Dertmann, J. Klimko, D. Oráč, A. Miškufová, T. Havlík, B. Friedrich, A combined pyro- and hydrometallurgical approach to recycle pyrolyzed lithium-ion battery black mass part 1: production of lithium concentrates in an electric arc furnace, Metals 10 (2020) 1069, https://doi.org/10.3390/met10081069.

[47] C. Stallmeister, M. Scheller, B. Friedrich, Slag design for pyrometallurgical metal recycling and targeted lithium slagging from lithium-ion batteries, in: Proceedings of the 8th Slag Valorisation Symposium. Presented at the 8th Slag Valorisation Symposium, Mechelen, Belgium, 2023.

[48] I.P. Swainson, M.T. Dove, W.W. Schmahl, A. Putnis, Neutron powder diffraction study of the åkermanite-gehlenite solid solution series, Phys. Chem. Miner. 19 (1992), https://doi.org/10.1007/BF00202107.

[49] T. Tawonezvi, M. Nomnqa, L. Petrik, B.J. Bladergroen, Recovery and recycling of valuable metals from spent lithium-ion batteries: a comprehensive review and analysis, Energies 16 (2023) 1365, https://doi.org/10.3390/en16031365.

[50] The European Parliament and the Council of the European Union, 2023. Regulation (EU) 2023/1542 concerning batteries and waste batteries. https://eur-lex.europa.eu/eli/reg/2023/1542/oj/eng (accessed on: 19.08.2024).

[51] J. Tytgat, The recycling efficiency of Li-ion EV batteries according to the European commission regulation, and the relation with the end-of-life vehicles directive recycling rate, World Electr. Veh. J. 6 (2013) 1039–1047.
[52] M. Vest, J. Zervos, R. Weyhe, B. Friedrich, Slag design for lithium recovery from spent batteries, in: International Workshop on Metal-Slag Interaction. Presented at the International Workshop on Metal-Slag Interaction, Yalta, Crimea - Ukraine, 2010, https://doi.org/10.13140/RG.2.1.3984.1525.
[53] A. Vezzini, Manufacturers, Materials and Recycling Technologies. Lithium-Ion Batteries, Elsevier, 2014, pp. 529–551, https://doi.org/10.1016/B978-0-444-59513-3.00023-6.
[54] R. Wagner-Wenz, A.-J. Van Zuilichem, L. Göllner-Völker, K. Berberich, A. Weidenkaff, L. Schebek, Recycling routes of lithium-ion batteries: a critical review of the development status, the process performance, and life-cycle environmental impacts, MRS Energy Sustain. 10 (2022) 1–34, https://doi.org/10.1557/s43581-022-00053-9.
[55] N. Wongnaree, T. Yingnakorn, N. Ma-Ud, L. Sriklang, S. Khumkoa, Recovery of valuable metals from leached solutions of black mass through precipitation method, Results. Eng. 25 (2025) 104190, https://doi.org/10.1016/j.rineng.2025.104190.
[56] X. Wu, J. Ma, J. Wang, X. Zhang, G. Zhou, Z. Liang, Progress, key issues, and future prospects for Li-ion battery recycling, Glob. Chall. 6 (2022) 2200067, https://doi.org/10.1002/gch2.202200067.
[57] X. Zeng, J. Li, N. Singh, Recycling of spent lithium-ion battery: a critical review, Crit. Rev. Environ. Sci. Technol. 44 (2014) 1129–1165, https://doi.org/10.1080/10643389.2013.763578.